Experimental evaluation of thermodynamic cost and speed limit in living cells via information geometry

Keita Ashida,[1] Kazuhiro Aoki,[2,3,4] and Sosuke Ito[1,5,6]

[1]*Universal Biology Institute, The University of Tokyo, 7-3-1 Hongo, Bunkyo-ku, Tokyo 113-0031, Japan*
[2]*Quantitative Biology Research Group, Exploratory Research Center on Life and Living Systems (ExCELLS),*
National Institutes of Natural Sciences, 5-1 Higashiyama, Myodaiji-cho, Okazaki, Aichi 444-8787, Japan
[3]*Division of Quantitative Biolny, National Institute for Basic Biology,*
National Institutes of Natural Sciences, 5-1 Higashiyama, Myodaiji-cho, Okazaki, Aichi 444-8787, Japan
[4]*Department of Basic Biology, School of Life Science,*
SOKENDAI (The Graduate University for Advanced Studies),
5-1 Higashiyama, Myodaiji-cho, Okazaki, Aichi 444-8787, Japan
[5]*Department of Physics, The University of Tokyo, 7-3-1 Hongo, Bunkyo-ku, Tokyo 113-0031, Japan*
[6]*JST, PRESTO, 4-1-8 Honcho, Kawaguchi, Saitama, 332-0012, Japan*

Chemical reactions are responsible for information processing in living cells, and their accuracy and speed have been discussed from a thermodynamic viewpoint [1–5]. The recent development in stochastic thermodynamics enables evaluating the thermodynamic cost of information processing [6–8]. However, because experimental estimation of the thermodynamic cost based on stochastic thermodynamics requires a sufficient number of samples [9], it is only estimated in simple living systems such as RNA folding [10] and F_1-ATPase [11] . Therefore, it is challenging to estimate the thermodynamic cost of information processing by chemical reactions in living cells. Here, we evaluated the thermodynamic cost and its efficiency of information processing in living systems at the single-cell level for the first time by establishing an information-geometric method to estimate them with a relatively small number of samples. We evaluated the thermodynamic cost of the extracellular signal-regulated kinase (ERK) phosphorylation from the time series of the fluorescence imaging data by calculating the intrinsic speed in information geometry. We also evaluated a thermodynamic efficiency based on the thermodynamic speed limit [8, 12, 13], and thus this paper reports the first experimental test of thermodynamic uncertainty relations in living systems. Our evaluation revealed the change of the efficiency under the conditions of different cell densities and its robustness to the upstream pathway perturbation. Because our approach is widely applicable to other signal transduction pathways such as the G-protein coupled receptor pathways for sensation [14], it would clarify efficient mechanisms of information processing in such a living system.

The Gibbs free energy change mainly drives information transmission in living cells, and its mechanism follows thermodynamic laws. For example, systems biology reveals a deep connection between information transmission accuracy and the Gibbs free energy change in a cell [1, 2]. In recent developments of stochastic thermodynamics [15] and chemical thermodynamics [16, 17], a similar connection occurs more deeply. The trade-off relations among speed, thermodynamic cost, and accuracy in a living cell have been proposed [3, 4], and its general thermodynamic bound of information processing in signal transduction has been discussed

in terms of Maxwell's demon [5, 18–20]. Moreover, as thermodynamic generalizations of uncertainty relations, thermodynamic trade-off relations have been intensively studied in terms of thermodynamic uncertainty relations [21, 22] and thermodynamic speed limits [8, 23–29]. These trade-off relations are mainly based on mathematical properties of the Fisher information [8, 12, 30], which gives a metric of information geometry [31]. Historically, information geometry has been considered as a possible choice of differential geometry for equilibrium thermodynamics [7, 32]. In recent years, information geometry meets nonequilibrium thermodynamics such as stochastic thermodynamics [8, 12, 33] and chemical thermodynamics [13], and it provides a unified framework to derive these trade-off relations in living systems [8, 12, 13]. While theoretical progress of thermodynamic trade-off relations has been intensively made for biological applications, the thermodynamic uncertainty relation has been experimentally tested only in artificial systems [34, 35]. An experimental test of thermodynamic trade-off relations in living systems has not been reported, and the thermodynamic speed limit has not been tested even in artificial systems.

This paper experimentally evaluated the thermodynamic cost by quantifying the Fisher information of time from the fluorescence imaging of the ERK phosphorylation in normal rat kidney epithelial (NRK-52E) cells. In information geometry, the Fisher information of time is regarded as the square of the intrinsic speed. This Fisher information is calculated from the time evolution of the phosphorylated ERK fraction, which can be experimentally measured by the Förster resonance energy transfer (FRET) signal. We also evaluated other information-geometric quantities for activation and inactivation processes from this Fisher information, and these information-geometric quantities illustrate the thermodynamic cost of the ERK phosphorylation, which is related to the Gibbs free energy change and the fluctuation-response ratio. We focused on the thermodynamic speed limit based on these information-geometric quantities and found that the efficiency ranges from 0.4 to 0.9 for the ERK phosphorylation in living NRK-52E cells. We quantified the thermodynamic variability for cell density changes and the perturbation of the upstream Raf pathway. While the cell density increases the thermodynamic cost and reduces efficiency, the Raf inhibitor

addition reduces the thermodynamic cost, but the efficiency is robust to the Raf inhibitor addition.

The information-geometric method proposed in this paper is generally applicable to switching dynamics between the active state and the inactive state. We consider the following chemical reaction

$$A_{\text{off}} \underset{k_{\text{off}}}{\overset{k_{\text{on}}(s')}{\rightleftarrows}} A_{\text{on}}, \tag{1}$$
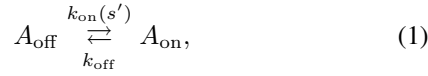
where A_{on} is an active state, A_{off} is an inactive state, s' is stimulus, and $k_{\text{on}}(s')$ and k_{off} are rate constants. Because $k_{\text{on}}(s')$ can depend on stimulus s', it causes a pulsatile response of A_{on} if this stimulus s' is excitable. This paper focuses on the ERK phosphorylation in the Ras-Raf-MEK-ERK pathway that shows a pulsatile response [36–38]. In Fig. 1a, we show the Ras-Raf-MEK-ERK pathway that relays extracellular stimuli such as growth factors from the plasma membrane to targets in the cytoplasm and nucleus. This three-tiered Raf-MEK-ERK mitogen-activated protein kinase (MAPK) cascade plays an essential role in various cellular processes, including cell proliferation, differentiation, and tumorigenesis [39]. Upon growth factor stimulation, the receptor tyrosine kinase (RTK) activates the Ras small GTPase at the plasma membrane, which recruits and activates the Raf. The activated Raf induces activation and phosphorylation of the MEK. The upstream kinase MEK phosphorylates the ERK to increase kinase activation of the ERK. The phosphorylated ERK is finally dephosphorylated by phosphatases, thereby shutting down the ERK activation. The phosphorylated MEK catalyzes a phosphate transfer from the adenosine triphosphate (ATP) to the ERK, and the Gibbs free energy difference of ATP hydrolysis thermodynamically drives this phosphorylation of the ERK [39, 40]. Here, A_{on} corresponds to a phosphorylated state of the ERK, A_{off} corresponds to a nonphosphorylated state of the ERK, and s' corresponds to the stimulus by upstream proteins in the Ras-Raf-MEK-ERK pathway, respectively. We try to estimate the thermodynamic cost of the ERK phosphorylation in living cells using the time series of the phosphorylated ERK fraction, which can be experimentally measured by the FRET technique at the single-cell level [37].

We discuss the thermodynamic cost estimation from the time series of the phosphorylated ERK fraction $P_1 = [A_{\text{on}}]/([A_{\text{on}}] + [A_{\text{off}}])$, where $[A_{\text{on}}]$ and $[A_{\text{off}}]$ are concentrations corresponding to A_{on} and A_{off}, respectively (see also Supplementary Note). In general, it is hard to estimate the Gibbs free energy change in living cells because it needs prior knowledge about the equilibrium concentration [16]. However, this equilibrium concentration is not estimated well from the time series of P_1. We propose a novel information-geometric method to estimate the thermodynamic cost from P_1, which does not require prior knowledge about the equilibrium concentration. Because the total concentration $[A_{\text{tot}}] = [A_{\text{off}}] + [A_{\text{on}}]$ is conserved, the nonphosphorylated and phosphorylated ERK fractions $P_0 = 1 - P_1 = [A_{\text{off}}]/[A_{\text{tot}}]$ and $P_1 = [A_{\text{on}}]/[A_{\text{tot}}]$ can be regarded as the probability distribution, and a Riemannian manifold can be introduced as the set of probability distributions in information geometry [31].

This method focuses on an intrinsic speed $ds/dt = \sqrt{ds^2/dt^2}$ on this manifold related to the thermodynamic cost, such as the Gibbs free energy change and the fluctuation-response ratio of the ERK phosphorylation [8, 12, 13]. The square of the intrinsic speed is given by the Fisher information of time

$$\frac{ds^2}{dt^2} = \sum_{i=0}^{1} P_i \left(\frac{d\ln P_i}{dt} \right)^2 = \sum_{i=0}^{1} \frac{1}{P_i} \left(\frac{dP_i}{dt} \right)^2. \tag{2}$$

Because ds^2/dt^2 only consists of the concentration fraction P_i and its change speed dP_i/dt, we can estimate it from the time series of P_1.

The square of the intrinsic speed can quantify the thermodynamic cost of ERK phosphorylation (see also Supplementary Note). Under near-equilibrium condition, we obtain $ds^2/dt^2 \simeq -(d\sigma/dt)/(2R[A_{\text{tot}}])$, where R is the gas constant, and σ is the entropy production that is the minus sign of the Gibbs free energy change over the temperature [13]. Then, the Fisher information of time is proportional to the entropy production rate change under near-equilibrium condition. Even for a system far from equilibrium, the square of the intrinsic speed gives the fluctuation-response ratio of the ERK phosphorylation. Let f_i be an observable of the ERK states, where $i = 0(i = 1)$ means the nonphosphorylated (phosphorylated) state. The square of the intrinsic speed ds^2/dt^2 is equal to the fluctuation-response ratio

$$\frac{ds^2}{dt^2} = \frac{|d_t\langle f \rangle_t|^2}{\text{Var}[f]_t}, \tag{3}$$

where $\langle f \rangle_t = \sum_i P_i(t) f_i$ is the mean value, $|d_t\langle f \rangle_t| = |d\langle f \rangle_t/dt|$ implies the time-response of the observable, and $\text{Var}[f]_t = \langle f^2 \rangle_t - \langle f \rangle_t^2$ implies the observable fluctuation. This relation is a consequence of the Cramér-Rao inequality for an efficient estimator, where any observable of a binary state can be regarded as an efficient estimator.

As shown in Fig. 1b, a pulsatile response consists of activation and inactivation processes, and we introduce information-geometric quantities of these processes as measures of the thermodynamic cost and the speed limit's efficiency (see also Supplementary Note). During the activation (inactivation) process, the phosphorylated ERK fraction P_1 is monotonically increasing (decreasing) in time. The activation (inactivation) starts at time $t_0 = t_{\text{ini}}$ ($t_0 = t_{\text{peak}}$) and ends at time $t_1 = t_{\text{peak}}$ ($t_1 = t_{\text{fin}}$). We here introduce three information-geometric quantities [7, 8], the action

$$\mathcal{C} = \frac{1}{2} \int_{t_0}^{t_1} dt \frac{ds^2}{dt^2}, \tag{4}$$

the length

$$\mathcal{L} = \int_{t_0}^{t_1} \sqrt{\frac{ds^2}{dt^2}} dt = 2\arccos\left[\sum_{i=0}^{1} \sqrt{P_i|_{t=t_0}\ P_i|_{t=t_1}} \right], \tag{5}$$

and the mean velocity

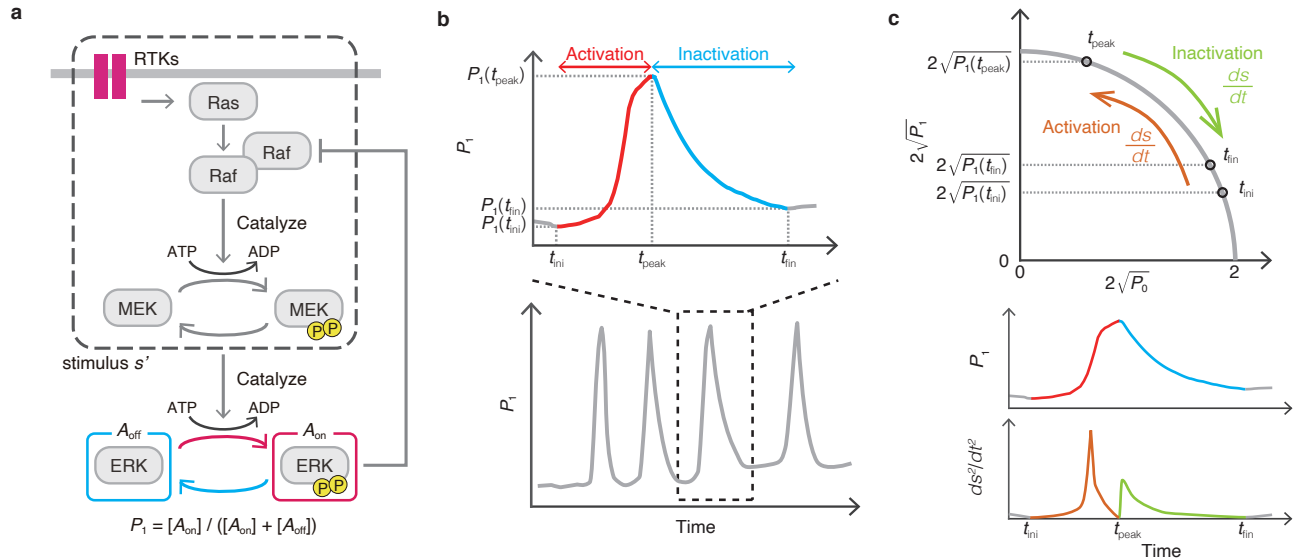$$\mathcal{V} = \frac{\mathcal{L}}{t_1 - t_0}, \tag{6}$$

Fig. 1: Schematic of the ERK phosphorylation, the time series of the phosphorylated ERK fraction P_1, and the square of the intrinsic speed ds^2/dt^2. **a** The Raf-MEK-ERK MAP pathway as an example of switching dynamics between the active state A_{on} and the inactive state A_{off}. The phosphorylated and nonphosphorylated ERKs correspond to A_{on} and A_{off}, respectively. The upstream proteins correspond to the stimulus s', and the Raf on the upstream pathway affects the phosphorylated ERK. **b** Typical behavior of the phosphorylated ERK fraction P_1 in the activation and inactivation processes. The time t_{ini} (t_{peak}) indicates the beginning of the activation (inactivation), and the time t_{peak} (t_{fin}) indicates the end of the activation (inactivation). **c** Schematic of the manifold in information geometry and the intrinsic speed ds/dt on this manifold. The activation and inactivation processes give at least two peaks in the time series of ds^2/dt^2, because $ds^2/dt^2 = 0$ at times t_{ini}, t_{peak}, and t_{fin}.

during the process from time t_0 to t_1. The action $\mathcal{C}$ quantifies the thermodynamic cost of the process because the action $\mathcal{C} \simeq \sigma|_{t=t_0}/(4R[A_{\mathrm{tot}}])$ is approximately proportional to the entropy production rate at time t_0 under near-equilibrium condition. Even for a system far from equilibrium, the action $\mathcal{C}$ can be interpreted as the thermodynamic cost in terms of the fluctuation-response ratio in Eq. (3) and becomes large if the observable change speed $|d_t\langle f\rangle_t|$ is relatively larger than its fluctuation $\sqrt{\mathrm{Var}[f]_t}$ during the process. The length $\mathcal{L}$ is given by twice the Bhattacharyya angle, which is a measure of a difference between two concentration fractions at time t_0 and time t_1. The mean velocity $\mathcal{V}$ quantifies the speed of the concentration fraction change during the process. In information geometry, $\mathcal{L}$ is regarded as the arc length of a circle in $2\sqrt{P_i}$ coordinate, and ds/dt is the intrinsic speed on this circle (see also Fig. 1c). From the Cauchy-Schwarz inequality, we obtain the thermodynamic speed limit [8]

$$\mathcal{L}^2 \leq 2\mathcal{C}(t_1 - t_0), \tag{7}$$

which is a trade-off relation between the thermodynamic cost $\mathcal{C}$ and the transition time $t_1 - t_0$ during the process. To quantify how much the thermodynamic cost converts into the concentration fraction change speed, we can consider the speed limit's efficiency [8]

$$\eta = \frac{\mathcal{L}^2}{2(t_1 - t_0)\mathcal{C}} = \frac{\mathcal{V}\mathcal{L}}{2\mathcal{C}}. \tag{8}$$

The efficiency η satisfies $0 \leq \eta \leq 1$, and $\eta = 1$ ($\eta = 0$) implies that this conversion is most efficient (inefficient). The efficiency becomes higher if the intrinsic speed is close to constant because $\eta = 1$ if and only if the intrinsic speed ds/dt is constant regardless of time, $(d/dt)|ds^2/dt^2| = 0$.

We experimentally measured the phosphorylated ERK fraction in living NRK-52E cells with the FRET-based ERK biosensor, the EKAREV-NLS (Fig. 2a) [41]. By comparing the fluorescence ratio of cells with the phosphorylated ERK fraction obtained from the western blotting (Fig. 2b), we quantified P_1 and the square of the intrinsic speed ds^2/dt^2 for the ERK activation ($p = \mathrm{a}$) and inactivation ($p = \mathrm{i}$) processes under the condition of different cell densities: 2.0×10^3 cells/cm^2 (low, $d = \mathrm{L}$), 2.0×10^4 cells/cm^2 (medium, $d = \mathrm{M}$), and 2.0×10^5 cells/cm^2 (high, $d = \mathrm{H}$), where the indices $p \in \{\mathrm{a},\mathrm{i}\}$ and $d \in \{\mathrm{L},\mathrm{M},\mathrm{H}\}$ regard the process and cell density, respectively. The pulses of the ERK activation were observed under these conditions (Fig. 2c and Supplementary Video 1), and the behavior of ds^2/dt^2 characterizes these conditions p and d (Fig. 2d). It reveals thermodynamic differences of the intracellular ERK activation under these conditions.

The information-geometric quantities $\{\mathcal{C}, \mathcal{L}, \mathcal{V}\}_d^p$ also differentiate these conditions (Fig. 3 and Extended Data Table 2). Firstly, we discuss the histogram of the action. The mean value of the action $\overline{\mathcal{C}_d^p}$ becomes larger as cell density increases $\overline{\mathcal{C}_{\mathrm{H}}^p} > \overline{\mathcal{C}_{\mathrm{M}}^p} > \overline{\mathcal{C}_{\mathrm{L}}^p}$ for both $p = \mathrm{a}$ and $p = \mathrm{i}$. It reflects the
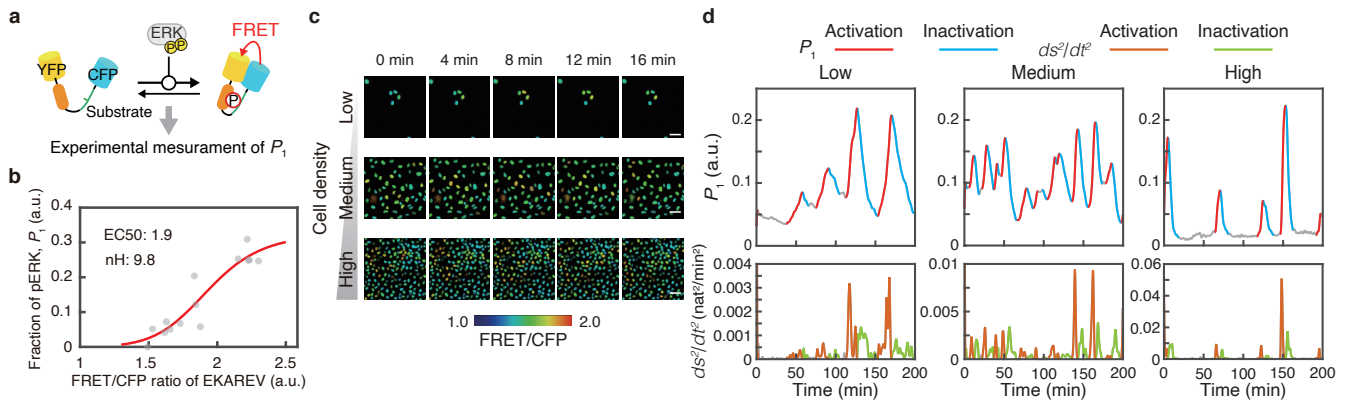
Fig. 2: The dynamics of the ERK phosphorylation under the conditions of different cell densities. **a** Schematic of the FRET-based ERK sensor. The phosphorylated ERK fraction P_1 can be measured from this FRET signal. **b** The relation between the FRET/CFP ratios of the EKAREV-NLS and the phosphorylated ERK fraction P_1. The red line indicates the fitted curve of the Hill equation. **c** Representative images of the phosphorylated ERK under the conditions of low, medium, and high cell densities. Scale bars indicate 50 μm. **d** Representative examples of the ERK phosphorylation dynamics under low (left), medium (middle), and high (right) cell densities. The unit (a.u.) indicates the arbitrary unit, and the unit (nat) indicates the natural unit of information.
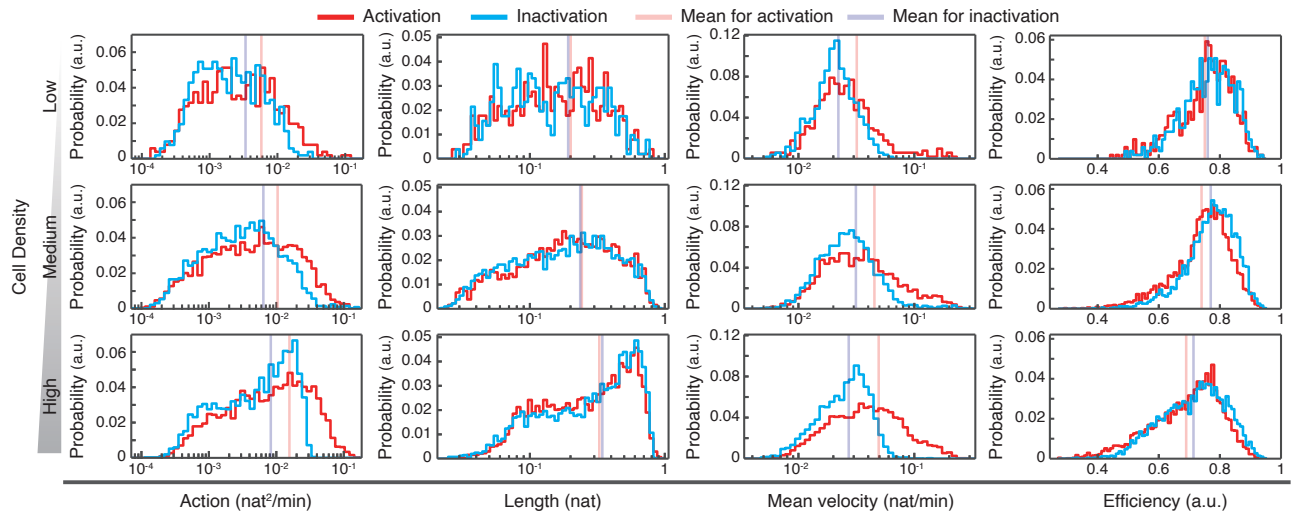
Fig. 3: The histograms of the action $\mathcal{C}$, length $\mathcal{L}$, mean velocity $\mathcal{V}$, and efficiency η under the conditions of different cell densities. The sample size, mean values, variances, and results of statistical tests are listed in Extended Data Table 1, 2.

fact that the speed under the condition of the high density appeared faster than the low density. The difference of $\overline{\mathcal{C}_d^p}$ between the high (medium) and low densities is at least twice ($\overline{\mathcal{C}_H^a}/\overline{\mathcal{C}_L^a} \simeq 2.7$, $\overline{\mathcal{C}_H^i}/\overline{\mathcal{C}_L^i} \simeq 2.4$). In comparison with the activation and inactivation processes, $\overline{\mathcal{C}_d^a}$ is approximately twice as much as $\overline{\mathcal{C}_d^i}$, and the distributions for the activation have longer tails than the inactivation. Because the action is a measure of the thermodynamic cost, these results suggest that the activation's thermodynamic cost is larger than the inactivation's one and becomes larger as cell density increases. Secondly, we discuss the histogram of the length. While the length does not

distinguish the activation process from the inactivation process, the mean value of the length $\overline{\mathcal{L}_d^p}$ differentiates the cell densities. It reflects the fact that the peak of the spike becomes higher as the cell density increases. Finally, we discuss the histogram of the mean velocity. The mean value of the mean velocity for the activation $\overline{\mathcal{V}_d^a}$ is larger than the inactivation $\overline{\mathcal{V}_d^i}$. It shows that the speed of the activation is faster than the inactivation.

From these information-geometric quantities $\{\mathcal{C}, \mathcal{L}, \mathcal{V}\}_d^p$, we obtained the speed limit's efficiency $\eta_d^p = \mathcal{V}_d^p \mathcal{L}_d^p / (2\mathcal{C}_d^p)$ (Fig. 3 right column). The mean value of the speed limit's

efficiency is almost $\overline{\eta_d^p} \simeq 0.7$ under these conditions, and the distribution of η_H^p shifted to lower than those of η_L^p and η_M^p (see also Extended Data Table 2). The efficiencies range between $\eta_d^p = 0.4$ and $\eta_d^p = 0.9$, and the distributions' shapes are biased to the higher efficiency. We can detect that the activation process is less efficient than the inactivation process $\eta_d^a < \eta_d^i$. We also find that the efficiency becomes worse in the higher cell density $\eta_H^p < \eta_L^p$. These results indicate that the process is accelerated under the higher cell density, and the activation process is also more accelerated than the inactivation process by the thermodynamic cost. This idea is supported by the histogram of $|d/dt(ds^2/dt^2)|$ (Extended Data Fig. 1), which becomes zero when $\eta = 1$. The mean values of $|d/dt(ds^2/dt^2)|$ for the activation and the high cell density are larger than that for the inactivation and the low cell density, respectively (Extended Data Table. 2). The scatter plot (Extended Data Fig. 2, see also Extended Data Table 4) suggests no correlation between η_d^p and $\{\mathcal{C}, \mathcal{V}\}_d^p$, while $\mathcal{V}$ and $\mathcal{C}$ seem to have a correlation. Because cell density modulates the ERK activation's excitability through both changes in basal and peak levels of the ERK phosphorylation [37], the cellular density could affect the efficiency of the pulsatile phosphorylation and the thermodynamic cost.

We confirm that these information-geometric quantities show the thermodynamic properties of the ERK phosphorylation by comparing the Raf inhibitor addition situation. The pulsatile dynamics of the ERK activation is generated by stochastic noise from the Raf and feedback loops [37, 39], and the Gibbs free energy difference of the ERK phosphorylation is induced by stimulus s' from the upstream pathway, including the Raf [39, 40]. Thus, the Raf inhibitor addition reduces the Gibbs free energy change of the ERK phosphorylation and these information-geometric quantities. To ensure these relationships, we measured the ERK phosphorylation dynamics under the Raf inhibitor (SB590885) addition and compared its dynamics with the original dynamics before adding the Raf inhibitor (Fig. 4). Of note, it is well-known that a low dose of the Raf inhibitor could paradoxically activate the ERK signaling through the Raf dimerization [42–44]. The condition of the cell density is medium in this experiment. The application of a low dose (100 nM) of the Raf inhibitor immediately activated the ERK, and the ERK activity demonstrated slower dynamics than that before the Raf inhibitor treatment and after the activation [37] (Fig. 4a and Supplementary Video 2). This result implies that the thermodynamic cost of the ERK phosphorylation is immediately increased when adding the Raf inhibitor. After the dynamics of the relaxation on the upstream pathways, the Raf inhibitor addition generally decreases the thermodynamic cost of the ERK phosphorylation.

In Fig. 4b, we show the histograms of these information-geometric quantities and the efficiency $\{\mathcal{C}, \mathcal{L}, \mathcal{V}, \eta\}_{d'}^p$ before ($d' = $ pre) and after ($d' = $ post) the Raf inhibitor addition, where the subscript $d' \in \{$pre, post$\}$ regards the Raf inhibitor addition. The mean value of the action $\overline{\mathcal{C}_{d'}^p}$ decreases when the Raf is inhibited $\overline{\mathcal{C}_{\text{pre}}^p} > \overline{\mathcal{C}_{\text{post}}^p}$, and the mean values differ by one order of magnitude (see also Extended Data Table 3). This result shows the Raf inhibitor addition reduces the thermodynamic cost of the ERK phosphorylation. The mean velocity and length also decrease when the Raf inhibitor is added, $\overline{\mathcal{V}_{\text{pre}}^p} > \overline{\mathcal{V}_{\text{post}}^p}$, and $\overline{\mathcal{L}_{\text{pre}}^p} > \overline{\mathcal{L}_{\text{post}}^p}$, while the transition time $t_1 - t_0$ becomes longer by the Raf inhibitor addition (Extended Data Fig. 3 and see also Extended Data Table 3). Surprisingly, the mean value of the efficiency is robust to the Raf inhibitor addition $\overline{\eta_{\text{pre}}^p} \simeq \overline{\eta_{\text{post}}^p}$, while the peak of the histogram can be decreased after adding the Raf inhibitor. Moreover, the efficiency $\eta_{d'}^p$ seems to have no correlation with $\mathcal{C}_{d'}^p$ nor $\mathcal{V}_{d'}^p$ (Extended Data Fig. 4 and see also Extended Data Table 4), and this robustness would not come from an artifact correlation between information-geometric quantities. The efficiency compensation of the ERK phosphorylation might exist when the upstream pathways are perturbed by the inhibitor.

In summary, we introduced information-geometric quantities as thermodynamic measures, and evaluated the speed limit's efficiency for the ERK phosphorylation dynamics in living cells at the single-cell level. Our method quantitatively clarifies the amount of information transferred in living systems based on information geometry and the conversion efficiency from the thermodynamic cost to the intrinsic speed, which complements other studies about measurements of informational quantities in biological systems such as the mutual information in signal transduction [46–48] and the Fisher information matrix on molecular networks [49, 50]. Our method is generally applicable to the activation process, and it widely exists in signaling pathways such as the G-protein coupled receptor pathways for sensation [14] and the receptor tyrosine kinase signaling pathways for cell proliferation [45]. For example, the state change from the active state A_{on} to the inactive state A_{off} in the G-protein coupled receptor corresponds to its conformational change by small rearrangements accompanying the ligand-binding. It is interesting to evaluate the speed limit's efficiency for other activation processes on an equal footing with this ERK phosphorylation in living NRK-52E cells. Our approach has great potential for other biological applications, which might clarify an efficient signal transduction mechanism and lead to novel insight into living systems as an information processing unit driven by the thermodynamic cost.

[1] Hopfield, J. J. Kinetic proofreading: a new mechanism for reducing errors in biosynthetic processes requiring high specificity. *Proc. Natl. Acad. Sci. USA* **71**, 4135–4139 (1974).

[2] Ninio, J. Kinetic amplification of enzyme discrimination. *Biochimie* **57**, 587–595 (1975).

[3] Lan, G., Sartori, P., Neumann, S., Sourjik, V. & Tu, Y. The energy–speed–accuracy trade-off in sensory adaptation. *Nat. Phys.* **8**, 422–428 (2012).

[4] Mehta, P. & Schwab, D. J. Energetic costs of cellular computation. *Proc. Natl. Acad. Sci. USA* **109**, 17978–17982 (2012).

[5] Ito, S. & Sagawa, T. Maxwell's demon in biochemical signal transduction with feedback loop. *Nat. Commun.* **6**, 1–6 (2015).

Fig. 4: The dynamics of the ERK phosphorylation under the Raf inhibitor addition. **a** Representative dynamics under the Raf inhibitor addition. The Raf inhibitor (100 nM of SB590885) was applied at 120 min. We set the pre-addition region as the period from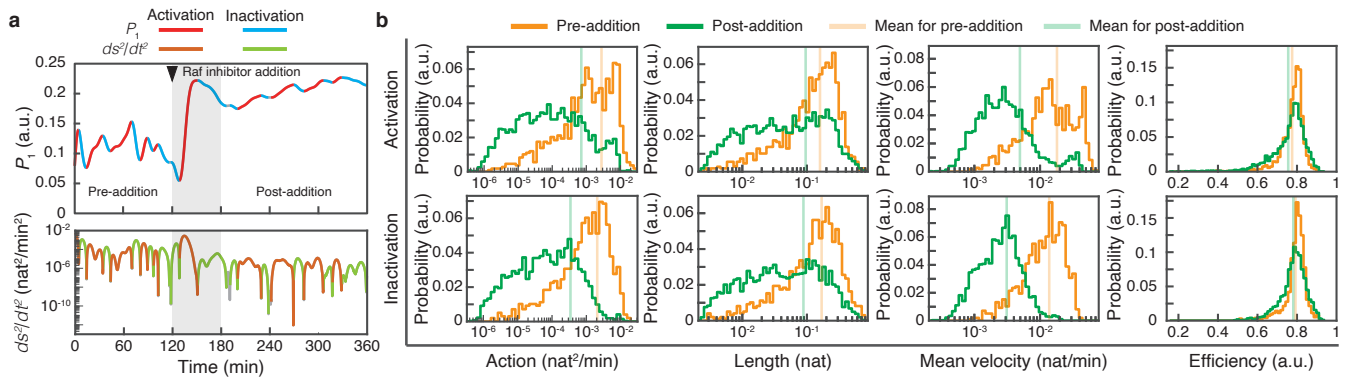 0 min to 120 min, and the post-addition region as the period after 180 min. **b** The histograms of the action $\mathcal{C}$, length $\mathcal{L}$, mean velocity $\mathcal{V}$, and the efficiency η before (pre-addition) and after (post-addition) adding the Raf inhibitor. The sample size, mean values, variances, and results of statistical tests are shown in Extended Data Table 1, 3.

[6] Parrondo, J. M., Horowitz, J. M. & Sagawa, T. Thermodynamics of information. *Nat. Phys.* **11**, 131–139 (2015).

[7] Crooks, G. E. Measuring thermodynamic length. *Phys. Rev. Lett.* **99**, 100602 (2007).

[8] Ito, S. Stochastic thermodynamic interpretation of information geometry. *Phys. Rev. Lett.* **121**, 030605 (2018).

[9] Ciliberto, S. Experiments in stochastic thermodynamics: Short history and perspectives. *Phys. Rev. X* **7**, 021051 (2017).

[10] Collin, D. et al. Verification of the Crooks fluctuation theorem and recovery of RNA folding free energies. *Nature* **437**, 231–234 (2005).

[11] Hayashi, K., Ueno, H., Iino, R. & Noji, H. Fluctuation theorem applied to F_1-ATPase. *Phys. Rev. Lett.* **104**, 218103 (2010).

[12] Ito, S. & Dechant, A. Stochastic time evolution, information geometry, and the Cramér-Rao bound. *Phys. Rev. X* **10**, 021056 (2020).

[13] Yoshimura, K. & Ito, S. Information geometric inequalities of chemical thermodynamics. Preprint at https://arxiv.org/abs/2005.08444 (2020).

[14] Luttrell, L. M. Reviews in molecular biology and biotechnology: transmembrane signaling by G protein-coupled receptors. *Mol. Biotechnol.* **39**, 239–264 (2008).

[15] Seifert, U. Stochastic thermodynamics, fluctuation theorems and molecular machines. *Rep. Prog. Phys.* **75**, 126001 (2012).

[16] Rao, R. & Esposito, M. Nonequilibrium thermodynamics of chemical reaction networks: wisdom from stochastic thermodynamics. *Phys. Rev. X* **6**, 041064 (2016).

[17] Ge, H. & Qian, H. Nonequilibrium thermodynamic formalism of nonlinear chemical reaction systems with Waage-Guldberg's law of mass action. *Chem. Phys.* **472**, 241–248 (2016).

[18] Ito, S. & Sagawa, T. Information thermodynamics on causal networks. *Phys. Rev. Lett.* **111**, 180603 (2013).

[19] Barato, A. C., Hartich, D. & Seifert, U. Efficiency of cellular information processing. *New J. Phys.* **16**, 103024 (2014).

[20] Sartori, P., Granger, L., Lee, C. F. & Horowitz, J. M. Thermodynamic costs of information processing in sensory adaptation. *PLoS Comput. Biol.* **10**, e1003974 (2014).

[21] Barato, A. C. & Seifert, U. Thermodynamic uncertainty relation for biomolecular processes. *Phys. Rev. Lett.* **114**, 158101 (2015).

[22] Horowitz, J. M. & Gingrich, T. R. Thermodynamic uncertainty relations constrain non-equilibrium fluctuations. *Nat. Phys.* **16**, 15–20 (2020).

[23] Shiraishi, N., Funo, K. & Saito, K. Speed limit for classical stochastic processes. *Phys. Rev. Lett.* **121**, 070601 (2018).

[24] Ashida, K. & Oka, K. Stochastic thermodynamic limit on *E. coli* adaptation by information geometric approach. *Biochem. Biophys. Res. Commun.* **508**, 690–694 (2019).

[25] Dechant, A. & Sakurai, Y. Thermodynamic interpretation of Wasserstein distance. Preprint at https://arxiv.org/abs/1912.08405 (2019).

[26] Gupta, D. & Busiello, D. M. Tighter thermodynamic bound on speed limit in systems with unidirectional transitions. Preprint at https://arxiv.org/abs/2009.11115 (2020).

[27] Zhang, Z., Guan, S. & Shi, H. Information geometry in the population dynamics of bacteria. *J. Stat. Mech.* **2020**, 073501 (2020).

[28] Falasco, G. & Esposito, M. Dissipation-time uncertainty relation. *Phys. Rev. Lett.* **125**, 120604 (2020).

[29] Nicholson, S. B., Garcia-Pintos, L. P., del Campo, A. & Green, J. R. Time–information uncertainty relations in thermodynamics. *Nat. Phys.* (2020).

[30] Dechant, A. Multidimensional thermodynamic uncertainty relations. *J. Phys. A* **52**, 035001 (2018).

[31] Amari, S. *Information Geometry and Its Applications.* (Springer, Japan, 2016).

[32] Ruppeiner, G. Riemannian geometry in thermodynamic fluctuation theory. *Rev. Mod. Phys.* **67**, 605 (1995).

[33] Ito, S., Oizumi, M. & Amari, S. Unified framework for the entropy production and the stochastic interaction based on information geometry. *Phys. Rev. Research* **2**, 033048 (2020).

[34] Pietzonka, P., Ritort, F. & Seifert, U. Finite-time generalization of the thermodynamic uncertainty relation. *Phys. Rev. E* **96**, 012101 (2017).

[35] Paneru, G., Dutta, S., Tlusty, T. & Pak, H. K. Reaching and violating thermodynamic uncertainty bounds in information engines. *Phys. Rev. E* **102**, 032126 (2020).

[36] Albeck, J. G., Mills, G. B. & Brugge, J. S. Frequency-modulated pulses of ERK activity transmit quantitative proliferation signals. *Mol. Cell* **49**, 249–261 (2013).

[37] Aoki, K. et al. Stochastic ERK activation induced by noise and cell-to-cell propagation regulates cell density-dependent prolif-

eration. *Mol. Cell* **52**, 529–540 (2013).

[38] Yang, J. M. et al. Integrating chemical and mechanical signals through dynamic coupling between cellular protrusions and pulsed ERK activation. *Nat. Commun.* **9**, 4673 (2018).

[39] Lavoie, H., Gagnon, J. & Therrien, M. ERK signalling: a master regulator of cell behaviour, life and fate. *Nat. Rev. Mol. Cell Biol.* **21**, 607–632 (2020).

[40] Knowles, J. R. Enzyme-catalyzed phosphoryl transfer reactions. *Annu. Rev. Biochem.* **49**, 877–919 (1980).

[41] Komatsu, N. et al. Development of an optimized backbone of FRET biosensors for kinases and GTPases. *Mol. Biol. Cell* **22**, 4647–4656 (2011).

[42] Hatzivassiliou, G. et al. RAF inhibitors prime wild-type RAF to activate the MAPK pathway and enhance growth. *Nature* **464**, 431–435 (2010).

[43] Heidorn, S. J. et al. Kinase-dead BRAF and oncogenic RAS cooperate to drive tumor progression through CRAF. *Cell* **140**, 209–221 (2010).

[44] Poulikakos, P. I. et al. RAF inhibitor resistance is mediated by dimerization of aberrantly spliced BRAF (V600E). *Nature* **480**, 387–390 (2011).

[45] Lemmon, M. A. & Schlessinger, J. Cell signaling by receptor tyrosine kinases. *Cell* **141**, 1117–1134 (2010).

[46] Mehta, P., Goyal, S., Long, T., Bassler, B. L. & Wingreen, N. S. Information processing and signal integration in bacterial quorum sensing. *Mol. Syst. Biol.* **5**, 325 (2009).

[47] Uda, S. et al. Robustness and compensation of information transmission of signaling pathways. *Science* **341**, 558–561 (2013).

[48] Selimkhanov, J. et al. Accurate information transmission through dynamic biochemical signaling networks. *Science* **346**, 1370–1373 (2014).

[49] Machta, B. B., Chachra, R., Transtrum, M. K. & Sethna, J. P. Parameter space compression underlies emergent theories and predictive models. *Science* **342**, 604–607 (2013).

[50] Singh, V. & Nemenman, I. Universal properties of concentration sensing in large ligand-receptor networks. *Phys. Rev. Lett.* **124**, 028101 (2020).

METHODS

Measurement of the phosphorylated ERK fraction

We measured the ERK phosphorylation, as previously described [51]. The EKAREV-NLS stable-expression NRK-52E cell lines (NRK-52E/ERKAREV-NLS cells) [37], were used, and the EKAREV-NLS is the genetically encoded ERK sensor used in Komatsu *et al.*, 2011 [41].

The NRK-52E/EKAREV-NLS cells were maintained with the Dulbecco's Modified Eagle Medium (DMEM; ThermoFisher), 10 % Fetal bovine serum (FBS; Sigma), and 10 µg/mL Blasticidin S (Invitrogen). The cells were seeded at a specific concentration (Low: 2.0×10^3 cells/cm^2, Medium: 2.0×10^4 cells/cm^2, High: 2.0×10^5 cells/cm^2) on glass-bottom dishes (IWAKI). One day after the seeding, the time-lapse imaging was performed. The culture media was replaced with the FluoroBrite (ThermoFisher), 5 % FBS (Sigma), and $1\times$ Glutamax (ThermoFisher) 3–6 hours before starting the time-lapse imaging. We used an inverted microscope (IX81; Olympus) equipped with a CCD camera (Cool-SNAP K4; Roper Scientific) and an excitation light source (Spectra-X light engine; Lumenncor). Optical filters were as follows: an FF01-438/24 excitation filter (Semrock), an XF2034 (455DRLP) dichroic mirror (Omega Optical), and two emission filters (FF01-483/32 for CFP and FF01-542/27 for YFP (Semrock)). Images were acquired every 20 sec (the exposure time was 100 ms) with binning 8×8 on MetaMorph software (Universal Imaging) with an IX2-ZDC laser-based autofocusing system (Olympus). A $\times 20$ lens (UPLSAPO 20X; Olympus, numerical aperture: 0.75) was used. The temperature and CO_2 concentration were maintained at 37°C and 5 % during the imaging with a stage top incubator (Tokai hit). For the Raf inhibitor experiment, the experiment was performed under the same condition as the medium cell density condition. We applied SB590885 (Selleck Chemicals) (a final concentration is 100 nM) 2 hours after the imaging initiation. The numbers of trials for each experimental condition are two.

We used the same relation between the FRET/CFP ratios of the EKAREV-NLS and the phosphorylated ERK fraction (pTpY-ERK2) from the western blotting in Fig. 2**b** as described previously [37]. In brief, the phosphorylated ERK fraction was quantified by the Phos-tag western blotting [52] in HeLa cells stimulated with different concentrations of 12-O-Tetradecanoylphorbol 13-acetate (TPA; Sigma) for 30 min to induce the ERK phosphorylation. Under the same condition, HeLa cells stably expressing EKAREV-NLS were imaged, followed by the quantification of the average FRET/CFP ratios. Finally, the FRET/CFP ratios were plotted as a function of the phosphorylated ERK fraction with the fitted curve of the Hill equation shown in Fig. 2**b** by the Solver Add-in in Excel (Microsoft).

Data analysis

For the imaging analysis, Fiji was used. The background was subtracted by the Subtract Background Tool, and after that, the nuclei were tracked with a custom-made tracking program. Only the cells which were tracked over the entire images were used for calculation of information-geometric quantities. The phosphorylated ERK fraction was calculated based on the FRET/CFP ratios with the Hill equation shown in Fig. 2**b**.

For analysis of the time-series phosphorylated ERK fractions, MATLAB 2019b (MathWorks) was used. The low-pass filter, whose cutoff frequency is 0.005 Hz, was used for the cell density experiment data with the designfilt function in the Signal Processing Toolbox to reduce the noise. The low-pass filter, whose cutoff frequency is $1/1200$ Hz, was used for the Raf inhibitor addition experiment data to detect the slower dynamics after the Raf inhibitor addition. We identified the activation and inactivation processes from the signs of the first and second derivatives. The first derivatives were numerically calculated using two data points of the phosphorylated fraction, and the second derivatives were numerically calculated using two data points of the first derivatives. We only calculated information-geometric quantities when the phosphorylated ERK fractions between maximum and minimum of the process over 0.01 for the density-experiment data and 0.001 for the Raf inhibitor addition experiment data. The square of an intrinsic speed ds^2/dt^2 was numerically calculated using two-points of the phosphorylated ERK fraction time series. The action $\mathcal{C}$, length $\mathcal{L}$, mean velocity $\mathcal{V}$, and efficiency η were calculated using ds^2/dt^2 according to the definitions. We used the set of time series for each cell in two trials for each experimental condition to make histograms.

For the statistical analysis, R (version 3.6.3; R project) was used. The Brunner-Munzel test was performed with the brunnermunzel.test function in the brunnermunzel library (version 1.4.1). The two-sample Kolmogorov–Smirnov test was performed with the ks.test function in the stats library (version 3.6.3). The Pearson correlation coefficients were calculated and tested by the cor.test function in the stats library (version 3.6.3). The Holm method was used to control the family-wise error rates with the p.adjust function in the stats library (version 3.6.3). The sample numbers are shown in Extended Data Table 1.

DATA AVAILABILITY

The data sets generated and analyzed during the current study are available from the corresponding author on reasonable request.

CODE AVAILABILITY

The source codes used in the current study are available from the corresponding author on reasonable request.

ACKNOWLEDGEMENTS

AUTHOR CONTRIBUTIONS

S. I. proposed the main method based on information geometry and designed the research. Kazuhiro Aoki performed experiments. Keita Ashida analyzed the data. All authors discussed the analytical results of the experiment and wrote the paper.

COMPETING INTERESTS STATEMENT

The authors declare no competing interests.

[51] Aoki, K. & Matsuda, M. Visualization of small GTPase activity with fluorescence resonance energy transfer-based biosensors. *Nat. Protoc.* **4**, 1623–1631 (2009).

[52] Kinoshita, E., Kinoshita-Kikuta, E., Takiyama, K. & Koike, T. Phosphate-binding tag, a new Tool to visualize phosphorylated proteins. *Mol. Cell. Proteom.* **5**, 749–757 (2006).

SUPPLEMENTARY INFORMATION

Supplementary Note: Chemical thermodynamics and information geometry for switching dynamics between the active and inactive states

This supplementary note briefly discusses a relationship between chemical thermodynamics and information geometry for switching dynamics between the active state A_{on} and the inactive state A_{off}. Let us consider the chemical reaction for the active and inactive states with stimulus s',

$$A_{\text{off}} \underset{k_{\text{off}}}{\overset{k_{\text{on}}(s')}{\rightleftarrows}} A_{\text{on}}, \tag{9}$$

where $k_{\text{on}}(s')$ and k_{off} are rate constants. Let $[A_{\text{off}}]$ and $[A_{\text{on}}]$ be concentrations of chemical states A_{off} and A_{on}, respectively. These concentrations are nonnegative, i.e., $[A_{\text{off}}] \geq 0$ and $[A_{\text{on}}] \geq 0$. In our study, A_{on} corresponds to the phosphorylated ERK state, A_{off} corresponds to the nonphosphorylated ERK state, and s' corresponds to upstream proteins' stimulus in the Ras-Raf-MEK-ERK pathway.

At first, we consider switching dynamics between the active and inactive states. The following rate equation describes the time evolution of concentrations $[A_{\text{off}}]$ and $[A_{\text{on}}]$,

$$\frac{d}{dt}[\boldsymbol{A}] = \mathsf{S}\boldsymbol{J}, \tag{10}$$

$$[\boldsymbol{A}] = \begin{pmatrix} [A_{\text{off}}] \\ [A_{\text{on}}] \end{pmatrix}, \tag{11}$$

$$\boldsymbol{J} = \begin{pmatrix} J_+ \\ J_- \end{pmatrix} = \begin{pmatrix} k_{\text{on}}(s')[A_{\text{off}}] \\ k_{\text{off}}[A_{\text{on}}] \end{pmatrix}, \tag{12}$$

$$\mathsf{S} = \begin{pmatrix} -1 & 1 \\ 1 & -1 \end{pmatrix}, \tag{13}$$

where t is time, the vector $\boldsymbol{J}$ implies the reaction rate, and S is called the stoichiometric matrix. Because the vector

$$\boldsymbol{l} = \begin{pmatrix} 1 \\ 1 \end{pmatrix}, \tag{14}$$

is in the left null space of S such that

$$\boldsymbol{l}^{\text{T}}\mathsf{S} = \boldsymbol{0}^{\text{T}}, \tag{15}$$

the sum of concentrations $[A_{\text{tot}}] = [A_{\text{on}}] + [A_{\text{off}}]$ is conserved

$$\frac{d[A_{\text{tot}}]}{dt} = \frac{d}{dt}(\boldsymbol{l}^{\text{T}}[\boldsymbol{A}]) = \boldsymbol{l}^{\text{T}}\mathsf{S}\boldsymbol{J} = \boldsymbol{0}^{\text{T}}\boldsymbol{J} = 0, \tag{16}$$

where $\boldsymbol{0}$ be the zero vector in two dimensions, and the symbol $^{\text{T}}$ implies the transpose of a vector. This conservation law $d[A_{\text{tot}}]/dt = 0$ corresponds to the conservation of the total mass. If we introduce the concentration fractions

$$\boldsymbol{P} = \begin{pmatrix} P_0 \\ P_1 \end{pmatrix} = \frac{1}{[A_{\text{tot}}]}[\boldsymbol{A}], \tag{17}$$

we have $P_0 \geq 0$, $P_1 \geq 0$ and $P_0 + P_1 = 1$. Then, (P_0, P_1) can be regarded as the probability distribution, and its dynamics are described by the master equation, which is equivalent to the rate equation (10),

$$\frac{d}{dt}\boldsymbol{P} = \mathsf{W}\boldsymbol{P}, \tag{18}$$

$$\mathsf{W} = \begin{pmatrix} -k_{\text{on}}(s') & k_{\text{off}} \\ k_{\text{on}}(s') & -k_{\text{off}} \end{pmatrix}, \tag{19}$$

where W is called the rate matrix. The equilibrium distribution is given by

$$\boldsymbol{P}^{\text{eq}} = \begin{pmatrix} P_0^{\text{eq}} \\ P_1^{\text{eq}} \end{pmatrix} = \frac{1}{k_{\text{on}}(s') + k_{\text{off}}} \begin{pmatrix} k_{\text{off}} \\ k_{\text{on}}(s') \end{pmatrix}, \tag{20}$$

which satisfies the detailed balance condition

$$k_{\mathrm{on}}(s')P_0^{\mathrm{eq}} = k_{\mathrm{off}}P_1^{\mathrm{eq}}. \tag{21}$$

This equilibrium distribution $\boldsymbol{P}^{\mathrm{eq}}$ generally depends on stimulus s'. Concentrations at equilibrium corresponding to $\boldsymbol{P}^{\mathrm{eq}}$ are given by

$$[\boldsymbol{A}]^{\mathrm{eq}} = \begin{pmatrix} [A_{\mathrm{off}}]^{\mathrm{eq}} \\ [A_{\mathrm{on}}]^{\mathrm{eq}} \end{pmatrix} = [A_{\mathrm{tot}}]\boldsymbol{P}^{\mathrm{eq}}. \tag{22}$$

The ratio of two rate constants $k_{\mathrm{on}}(s')/k_{\mathrm{off}}$ implies a thermodynamic property of the system. This fact is known as the local detailed balance condition such that

$$\frac{k_{\mathrm{on}}(s')}{k_{\mathrm{off}}} = \exp\left[\frac{\mu_{\mathrm{off}}^{\circ} - \mu_{\mathrm{on}}^{\circ}}{RT}\right], \tag{23}$$

where R is the gas constant, T is the temperature of the solvent, and $\mu_{\mathrm{on}}^{\circ}$ and $\mu_{\mathrm{off}}^{\circ}$ are standard chemical potentials corresponding to the active and inactive states. We now define the chemical potentials $\mu_{\mathrm{on}}([A_{\mathrm{on}}])$ and $\mu_{\mathrm{off}}([A_{\mathrm{off}}])$ as

$$\mu_{\mathrm{on}}([A_{\mathrm{on}}]) = \mu_{\mathrm{on}}^{\circ} + RT\ln[A_{\mathrm{on}}], \tag{24}$$

$$\mu_{\mathrm{off}}([A_{\mathrm{off}}]) = \mu_{\mathrm{off}}^{\circ} + RT\ln[A_{\mathrm{off}}]. \tag{25}$$

The local detailed balance condition (23) can be regarded as the equivalence of the chemical potential at equilibrium

$$\mu_{\mathrm{on}}([A_{\mathrm{on}}]^{\mathrm{eq}}) = \mu_{\mathrm{off}}([A_{\mathrm{off}}]^{\mathrm{eq}}). \tag{26}$$

If we define the vector of the chemical potential at equilibrium as

$$\boldsymbol{\mu}^{\mathrm{eq}} = \begin{pmatrix} \mu_{\mathrm{on}}([A_{\mathrm{on}}]^{\mathrm{eq}}) \\ \mu_{\mathrm{off}}([A_{\mathrm{off}}]^{\mathrm{eq}}) \end{pmatrix} = \mu_{\mathrm{on}}([A_{\mathrm{on}}]^{\mathrm{eq}})\boldsymbol{l}, \tag{27}$$

this vector is in the left null space of S, i.e., $\boldsymbol{\mu}^{\mathrm{eq}\,\mathrm{T}}\mathsf{S} = \boldsymbol{0}^{\mathrm{T}}$. Then, the quantity $\boldsymbol{\mu}^{\mathrm{eq}\,\mathrm{T}}[\boldsymbol{A}]$ is conserved,

$$\frac{d}{dt}\left(\boldsymbol{\mu}^{\mathrm{eq}\,\mathrm{T}}[\boldsymbol{A}]\right) = \boldsymbol{\mu}^{\mathrm{eq}\,\mathrm{T}}\mathsf{S}\boldsymbol{J} = 0. \tag{28}$$

Next, we discuss the chemical thermodynamics of a dilute solution with the temperature T kept constant. The Gibbs free energy per unit volume $G([\boldsymbol{A}])$ is defined as

$$G([\boldsymbol{A}]) = \mu_{\mathrm{on}}([A_{\mathrm{on}}])[A_{\mathrm{on}}] + \mu_{\mathrm{off}}([A_{\mathrm{off}}])[A_{\mathrm{off}}] - RT[A_{\mathrm{tot}}] + G_0, \tag{29}$$

where G_0 is a constant. This Gibbs free energy $G([\boldsymbol{A}])$ satisfies the relations in chemical thermodynamics,

$$\frac{\partial G([\boldsymbol{A}])}{\partial[A_{\mathrm{on}}]} = \mu_{\mathrm{on}}([A_{\mathrm{on}}]), \tag{30}$$

$$\frac{\partial G([\boldsymbol{A}])}{\partial[A_{\mathrm{off}}]} = \mu_{\mathrm{off}}([A_{\mathrm{off}}]). \tag{31}$$

From Eq. (28), we obtain

$$\boldsymbol{\mu}^{\mathrm{eq}\,\mathrm{T}}[\boldsymbol{A}] = \boldsymbol{\mu}^{\mathrm{eq}\,\mathrm{T}}[\boldsymbol{A}]^{\mathrm{eq}}, \tag{32}$$

and therefore the Gibbs free energy at equilibrium $G([\boldsymbol{A}]^{\mathrm{eq}})$ is expressed as

$$G([\boldsymbol{A}]^{\mathrm{eq}}) = \mu_{\mathrm{on}}([A_{\mathrm{on}}]^{\mathrm{eq}})[A_{\mathrm{on}}]^{\mathrm{eq}} + \mu_{\mathrm{off}}([A_{\mathrm{off}}]^{\mathrm{eq}})[A_{\mathrm{off}}]^{\mathrm{eq}} - RT[A_{\mathrm{tot}}]^{\mathrm{eq}} + G_0 \tag{33}$$

$$= \mu_{\mathrm{on}}([A_{\mathrm{on}}]^{\mathrm{eq}})[A_{\mathrm{on}}] + \mu_{\mathrm{off}}([A_{\mathrm{off}}]^{\mathrm{eq}})[A_{\mathrm{off}}] - RT[A_{\mathrm{tot}}]^{\mathrm{eq}} + G_0. \tag{34}$$

The Gibbs free energy difference $G([\boldsymbol{A}]) - G([\boldsymbol{A}]^{\mathrm{eq}})$ is given by

$$G([\boldsymbol{A}]) - G([\boldsymbol{A}]^{\mathrm{eq}}) = RT\left([A_{\mathrm{on}}]\ln\frac{[A_{\mathrm{on}}]}{[A_{\mathrm{on}}]^{\mathrm{eq}}} + [A_{\mathrm{off}}]\ln\frac{[A_{\mathrm{off}}]}{[A_{\mathrm{off}}]^{\mathrm{eq}}} + [A_{\mathrm{on}}]^{\mathrm{eq}} + [A_{\mathrm{off}}]^{\mathrm{eq}} - [A_{\mathrm{on}}] - [A_{\mathrm{off}}]\right). \tag{35}$$

If we use the definition of the f-divergence

$$D_f([\boldsymbol{A}]||[\boldsymbol{A}]^{\text{eq}}) = \left([A_{\text{on}}] \ln \frac{[A_{\text{on}}]}{[A_{\text{on}}]^{\text{eq}}} + [A_{\text{off}}] \ln \frac{[A_{\text{off}}]}{[A_{\text{off}}]^{\text{eq}}} + [A_{\text{on}}]^{\text{eq}} + [A_{\text{off}}]^{\text{eq}} - [A_{\text{on}}] - [A_{\text{off}}] \right), \tag{36}$$

which is the generalization of the Kullback-Leibler divergence for the positive measure space, the Gibbs free energy difference is given by

$$\frac{G([\boldsymbol{A}]) - G([\boldsymbol{A}]^{\text{eq}})}{RT} = D_f([\boldsymbol{A}]||[\boldsymbol{A}]^{\text{eq}}). \tag{37}$$

From the nonnegativity of the f-divergence $D_f([A]||[A]^{\text{eq}}) \geq 0$, we obtain

$$G([\boldsymbol{A}]) \geq G([\boldsymbol{A}]^{\text{eq}}), \tag{38}$$

which implies that the Gibbs free energy at equilibrium takes the smallest value. If we consider the conservation of the total mass $[A_{\text{on}}]^{\text{eq}} + [A_{\text{on}}]^{\text{eq}} = [A_{\text{on}}] + [A_{\text{on}}]$ and introduce the probability distributions $\boldsymbol{P}$ and $\boldsymbol{P}^{\text{eq}}$, the f-divergence is rewritten as the Kullback-Leibler divergence,

$$D_{\text{KL}}(\boldsymbol{P}||\boldsymbol{P}^{\text{eq}}) = \sum_{i=0}^{1} P_i \ln \frac{P_i}{P_i^{\text{eq}}} = \frac{1}{[A_{\text{tot}}]} D_f([\boldsymbol{A}]||[\boldsymbol{A}]^{\text{eq}}). \tag{39}$$

The time derivative of the Gibbs free energy is also given by the f-divergences

$$\frac{dG([\boldsymbol{A}])}{dt} = \mu_{\text{on}}([A_{\text{on}}])\frac{d[A_{\text{on}}]}{dt} + \mu_{\text{off}}([A_{\text{off}}])\frac{d[A_{\text{off}}]}{dt} \tag{40}$$

$$= (J_+ - J_-) \left[\mu_{\text{on}}([A_{\text{on}}]) - \mu_{\text{off}}([A_{\text{off}}]) \right] \tag{41}$$

$$= -RT \left[J_+ \ln \frac{J_+}{J_-} + J_- \ln \frac{J_-}{J_+} \right] \tag{42}$$

$$= -RT[D_f(J_+||J_-) + D_f(J_-||J_+)], \tag{43}$$

$$D_f(J_+||J_-) = J_+ \ln \frac{J_+}{J_-} + J_- - J_+, \tag{44}$$

$$D_f(J_-||J_+) = J_- \ln \frac{J_-}{J_+} + J_+ - J_-, \tag{45}$$

where we used the local detailed balance condition (23), which is equivalent to $\mu_{\text{on}}([A_{\text{on}}]) - \mu_{\text{off}}([A_{\text{off}}]) = RT \ln(J_-/J_+)$. From the nonnegativity of the f-divergence, we obtain

$$\frac{dG([\boldsymbol{A}])}{dt} \leq 0. \tag{46}$$

The entropy production $\sigma([\boldsymbol{A}])$ is defined as

$$\sigma([\boldsymbol{A}]) = -\frac{1}{T}\frac{dG}{dt}. \tag{47}$$

Therefore, $dG([\boldsymbol{A}])/dt \leq 0$ can be regarded as the second law of thermodynamics

$$\sigma([\boldsymbol{A}]) \geq 0. \tag{48}$$

We here introduce information geometry. In information geometry, the square of line element ds^2 is given by the 2nd order Taylor expansion of the Kullback-Leibler divergence

$$ds^2 = 2D_{\text{KL}}(\boldsymbol{P} + d\boldsymbol{P}||\boldsymbol{P}) + O(d\boldsymbol{P}^3) \tag{49}$$

$$= \sum_{i=0}^{1} \frac{(dP_i)^2}{P_i} \tag{50}$$

$$= \sum_{i=0}^{1} P_i (d \ln P_i)^2, \tag{51}$$

where $d\boldsymbol{P}$ is an infinitesimal difference of two probabilities, which satisfies $\sum_i dP_i = 0$. The Fisher information of time is also defined as

$$\frac{ds^2}{dt^2} = \sum_{i=0}^{1} P_i \left(\frac{d \ln P_i}{dt} \right)^2, \tag{52}$$

and its square root implies the intrinsic speed $ds/dt = \sqrt{ds^2/dt^2}$ in information geometry. We can also introduce information geometry for chemical reaction networks. The square of line element for chemical reaction networks ds^2_{chem} is given by the 2nd order Taylor expansion of the f-divergence

$$ds^2_{\text{chem}} = 2D_f([\boldsymbol{A}] + d[\boldsymbol{A}] || [\boldsymbol{A}]) + O(d[\boldsymbol{A}]^3) \tag{53}$$

$$= \frac{(d[A_{\text{on}}])^2}{[A_{\text{on}}]} + \frac{(d[A_{\text{off}}])^2}{[A_{\text{off}}]} \tag{54}$$

We obtain the relation between two geometries ds^2 and ds^2_{chem} as

$$ds^2 = \frac{1}{[A_{\text{tot}}]} ds^2_{\text{chem}} \tag{55}$$

$$\frac{ds^2}{dt^2} = \frac{1}{[A_{\text{tot}}]} \frac{ds^2_{\text{chem}}}{dt^2} \tag{56}$$

$$\tag{57}$$

Because the f-divergence is related to the Gibbs free energy, we can consider a thermodynamic interpretation of information geometry. Under near-equilibrium condition $[\boldsymbol{A}] = [\boldsymbol{A}]^{\text{eq}} + d[\boldsymbol{A}]$, we have

$$ds^2 \simeq \frac{2}{[A_{\text{tot}}]} D_f([\boldsymbol{A}]^{\text{eq}} + d[\boldsymbol{A}] || [\boldsymbol{A}]^{\text{eq}}) \tag{58}$$

$$= 2 \frac{G([\boldsymbol{A}]) - G([\boldsymbol{A}]^{\text{eq}})}{RT[A_{\text{tot}}]}. \tag{59}$$

Therefore, ds^2 can be interpreted as the Gibbs free energy difference under near-equilibrium condition. We also show that the Fisher information of time ds^2/dt^2 is given by

$$\frac{ds^2}{dt^2} = \frac{1}{[A_{\text{tot}}]} \left[\frac{d \ln[A_{\text{on}}]}{dt} \frac{d[A_{\text{on}}]}{dt} + \frac{d \ln[A_{\text{off}}]}{dt} \frac{d[A_{\text{off}}]}{dt} \right] \tag{60}$$

$$= \frac{1}{RT[A_{\text{tot}}]} \frac{d \left(\mu_{\text{on}}([A_{\text{on}}]) - \mu_{\text{off}}([A_{\text{off}}]) \right)}{dt} (J_+ - J_-) \tag{61}$$

$$= -\frac{1}{RT[A_{\text{tot}}]} \frac{d\mathcal{F}}{dt} \mathcal{J}, \tag{62}$$

where the flow is defined as $\mathcal{J} = J_+ - J_-$ and the force is defined as $\mathcal{F} = \mu_{\text{off}}([A_{\text{off}}]) - \mu_{\text{on}}([A_{\text{on}}]) = RT \ln(J_+/J_-)$. In this notation, the entropy production rate is given by $\sigma = \mathcal{F}\mathcal{J}/T$. In terms of the entropy production rate, the Fisher information of time is given by

$$\frac{ds^2}{dt^2} = -\frac{1}{2R[A_{\text{tot}}]} \frac{d\sigma}{dt} + \frac{1}{2RT[A_{\text{tot}}]} \left(\frac{d\mathcal{J}}{dt} \mathcal{F} - \frac{d\mathcal{F}}{dt} \mathcal{J} \right). \tag{63}$$

Under near-equilibrium condition $J_+ \simeq J_-$, we have $\mathcal{J} \simeq L\mathcal{F}$ with the Onsager's coefficient $L = RT/(k_{\text{off}}[A_{\text{on}}]^{\text{eq}})$ and

$$\frac{d\mathcal{J}}{dt} \mathcal{F} - \frac{d\mathcal{F}}{dt} \mathcal{J} \simeq 0. \tag{64}$$

Thus, the Fisher information of time gives the time derivative of the entropy production rate under near-equilibrium condition

$$\frac{ds^2}{dt^2} \simeq -\frac{1}{2R[A_{\text{tot}}]} \frac{d\sigma}{dt}. \tag{65}$$

We also discuss a thermodynamic meaning of the action for a transition from time $t = t_0$ to $t = t_1$, defined as

$$\mathcal{C} = \frac{1}{2} \int_{t_0}^{t_1} dt \frac{ds^2}{dt^2}. \tag{66}$$

Under near-equilibrium condition, we obtain

$$\mathcal{C} \simeq \frac{\sigma|_{t=t_0} - \sigma|_{t=t_1}}{4R[A_{\text{tot}}]}. \tag{67}$$

In a relaxation process, the system can be in equilibrium at the final time $t = t_1$, and the entropy production rate vanishes at the final time $\sigma|_{t=t_1} \simeq 0$. Therefore, the action can be proportional to the entropy production rate at the initial time $t = t_0$,

$$\mathcal{C} \simeq \frac{\sigma|_{t=t_0}}{4R[A_{\text{tot}}]}, \tag{68}$$

if the system is under near-equilibrium condition, and reach equilibrium at the final time $t = t_1$. That is why we regard the action $\mathcal{C}$ as a thermodynamic cost. In an experiment of the FRET measurement, we can easily estimate the Fisher information of time ds^2/dt^2 because it only consists of measurable quantities, i.e., the nonphosphorylated and phosphorylated ERK fractions P_0 and P_1 and its change speed dP_0/dt and dP_1/dt. On the other hand, it is hard to measure the Gibbs free energy G itself because we need prior knowledge about concentrations at equilibrium $[A_{\text{on}}]^{\text{eq}}$ and $[A_{\text{off}}]^{\text{eq}}$ to estimate G. It is also hard to measure the entropy production rate σ because we need prior knowledge about the rate constants $k_{\text{on}}(s')$ and k_{off} to estimate σ via J_+ and J_-.

Information theoretically, we can discuss the meaning of ds^2/dt^2 even for a system far from equilibrium. We here introduce the observable (f_0, f_1) corresponding to (P_0, P_1), and its ensemble average is defined as $\langle f \rangle_t = P_0(t)f_0 + P_1(t)f_1$. The square of the time derivative of $\langle f \rangle_t$ is given by

$$\left(\frac{d}{dt} \langle f \rangle_t \right)^2 = \left(f_0 \frac{dP_0}{dt} + f_1 \frac{dP_1}{dt} \right)^2 \tag{69}$$

$$= (f_0 - f_1)^2 \left(\frac{dP_0}{dt} \right)^2, \tag{70}$$

which implies the time-response of the observable. The variance of the observable is given by

$$\text{Var}[f]_t = \langle f^2 \rangle_t - \langle f \rangle_t^2 \tag{71}$$

$$= f_0^2 P_0 + f_1^2 (1 - P_0) - (f_0 P_0 + f_1 (1 - P_0))^2 \tag{72}$$

$$= (f_0 - f_1)^2 P_0 (1 - P_0), \tag{73}$$

which is the fluctuation of the observable. Thus, the fluctuation-response ratio is calculated as

$$\frac{\left(\frac{d}{dt} \langle f \rangle_t \right)^2}{\text{Var}[f]_t} = \frac{1}{P_0(1 - P_0)} \left(\frac{dP_0}{dt} \right)^2 \tag{74}$$

$$= \left(\frac{1}{P_0} + \frac{1}{P_1} \right) \left(\frac{dP_0}{dt} \right)^2 \tag{75}$$

$$= \frac{1}{P_0} \left(\frac{dP_0}{dt} \right)^2 + \frac{1}{P_1} \left(\frac{dP_1}{dt} \right)^2 \tag{76}$$

$$= \frac{ds^2}{dt^2}. \tag{77}$$

Therefore, the Fisher information of time implies the fluctuation-response ratio even for a system far from equilibrium.

We finally discuss the length $\mathcal{L}$ defined as

$$\mathcal{L} = \int_{t_0}^{t_1} dt \sqrt{\frac{ds^2}{dt^2}}. \tag{78}$$

We here introduce the change of variables $\sqrt{P_0(t)} = \cos\theta(t)$ and $\sqrt{P_1(t)} = \sin\theta(t)$ which satisfies the normalization of the probability $P_0(t) + P_1(t) = 1$. Then, the Fisher information of time is given by

$$\frac{ds^2}{dt^2} = \frac{1}{[\cos\theta(t)]^2}\left(\frac{d}{dt}[\cos\theta(t)]^2\right)^2 + \frac{1}{[\sin\theta(t)]^2}\left(\frac{d}{dt}[\sin\theta(t)]^2\right)^2 \tag{79}$$

$$= 4\left(\frac{d\theta}{dt}\right)^2, \tag{80}$$

which implies that ds^2 gives a differential geometry of the circle of radius 2. Thus, the length is calculated as

$$\mathcal{L} = 2\int_{t_0}^{t_1} dt \left|\frac{d\theta}{dt}\right| \geq 2|\theta(t_1) - \theta(t_0)| = \mathcal{D}. \tag{81}$$

The lower bound $\mathcal{D}$ is the geodesic length on the circle of radius 2. If we assume that the time evolution of P_1 from time t_0 to t_1 is monotonic, the equality holds $\mathcal{L} = \mathcal{D}$. In the main text, we consider $\mathcal{L} = \mathcal{D}$ for the activation and inactivation processes because P_1 in the activation (inactivation) process is monotonically increasing (decreasing) in time. From the identity

$$\cos|\theta(t_1) - \theta(t_0)| = \cos\theta(t_0)\cos\theta(t_1) + \sin\theta(t_0)\sin\theta(t_1), \tag{82}$$

the length can be calculated as

$$\mathcal{D} = 2\arccos\left[\sqrt{P_0(t_0)}\sqrt{P_0(t_1)} + \sqrt{P_1(t_0)}\sqrt{P_1(t_1)}\right], \tag{83}$$

where the angle $|\theta(t_1) - \theta(t_0)| = \arccos\left[\sqrt{P_0(t_0)}\sqrt{P_0(t_1)} + \sqrt{P_1(t_0)}\sqrt{P_1(t_1)}\right]$ is known as the Bhattacharyya angle.
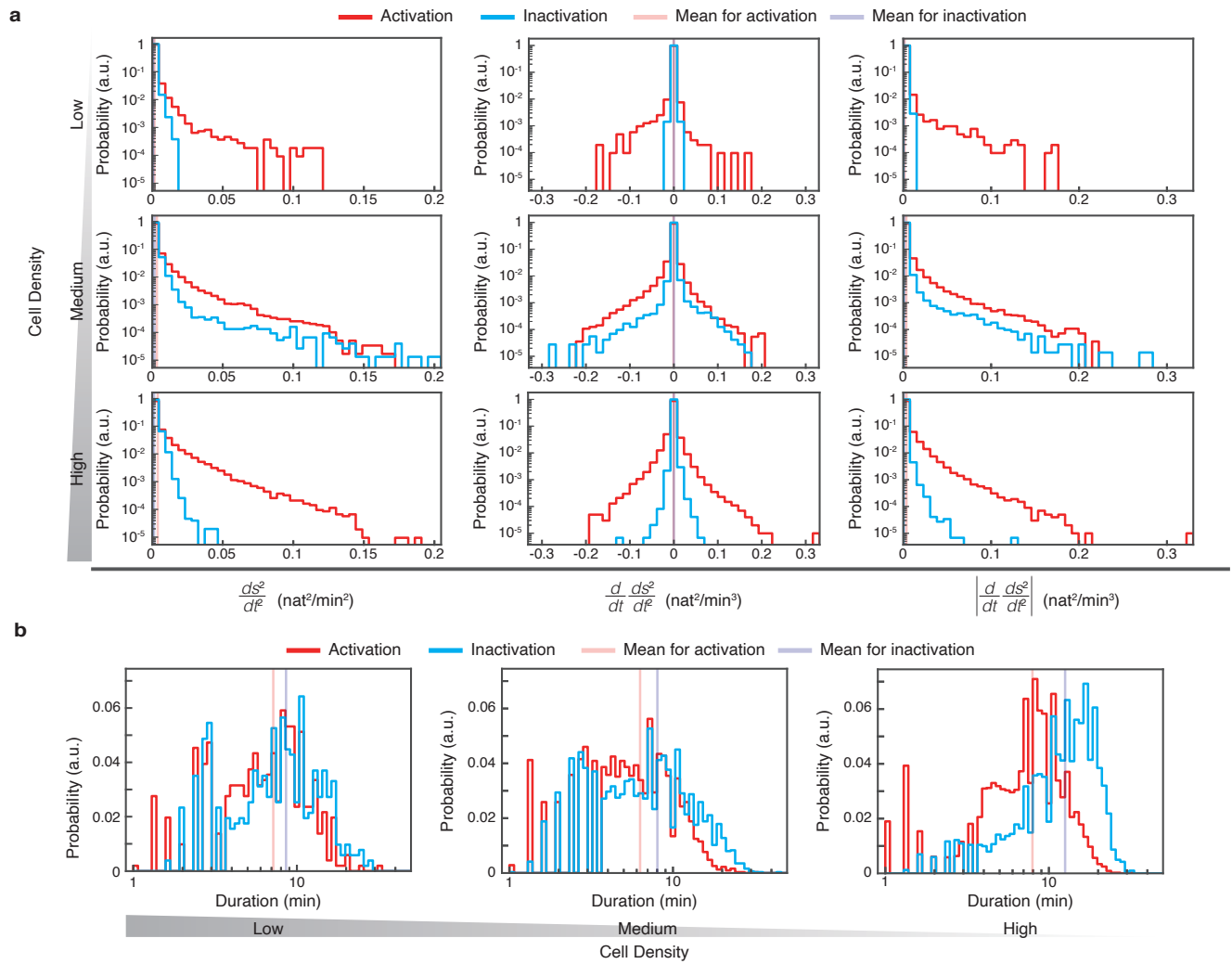
Extended Data Figure 1: The histograms of the square of the intrinsic speed and related quantities at the low, medium, and high cell densities. **a** The histograms of ds^2/dt^2, $d/dt(ds^2/dt^2)$, and $\left|d/dt(ds^2/dt^2)\right|$ at each cell density. **b** The histograms of the duration $(t_1 - t_0)$ of the activation and inactivation processes under each cell density. The mean values, variances, and results of statistical tests are listed in Extended Data Table 2.
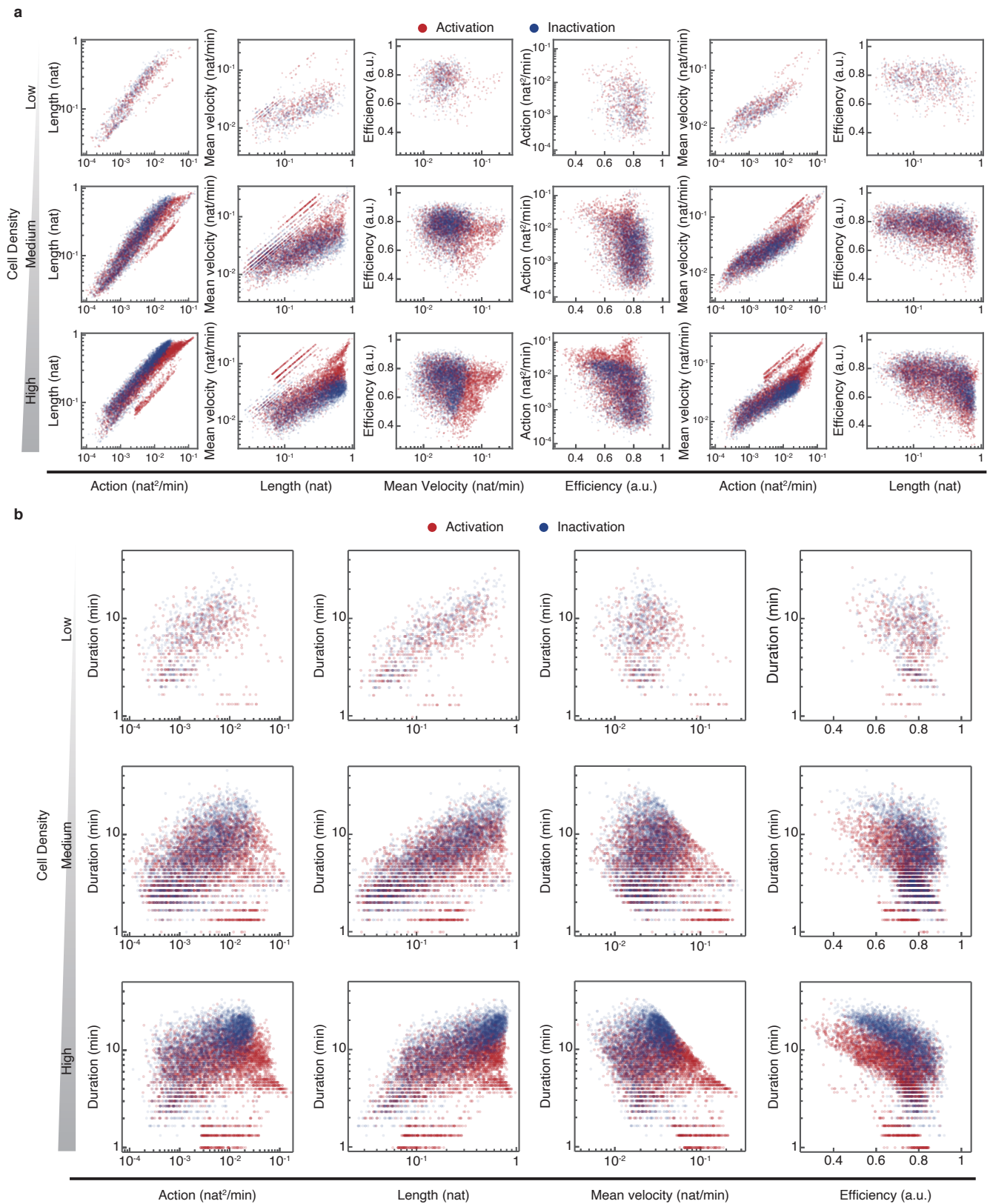
Extended Data Figure 2: The correlation between two information-geometric quantities at each cell density. **a** The scatter plots of the action $\mathcal{C}$, the length $\mathcal{L}$, the mean velocity $\mathcal{V}$, and the efficiency η. **b** The scatter plots of the duration $t_1 - t_0$ versus information-geometric quantity $(\mathcal{C}, \mathcal{V}, \eta)$. The Pearson correlation coefficients and results of statistical tests are listed in Extended Data Table 4.
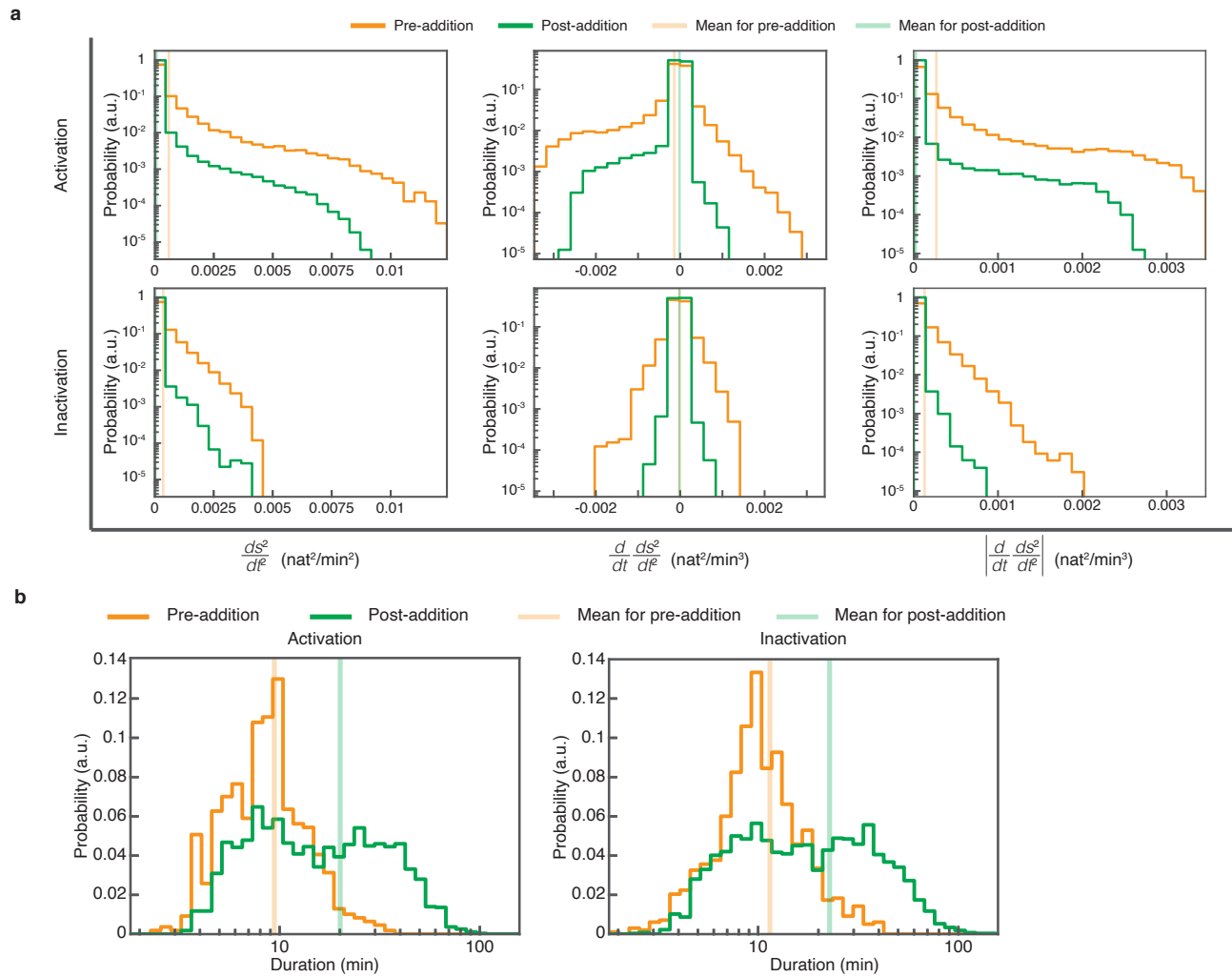
Extended Data Figure 3: The histograms of the square of the intrinsic speed and related quantities before and after the Raf inhibitor addition. **a** The histograms of ds^2/dt^2, $d/dt(ds^2/dt^2)$, and $\left|d/dt(ds^2/dt^2)\right|$ of the activation and inactivation processes before (pre-addition) and after (post-addition) the Raf inhibitor addition. **b** The histograms of the duration $t_1 - t_0$ of the activation and inactivation process before (pre-addition) and after (post-addition) the Raf inhibitor addition. The mean values, variances, and results of statistical tests are listed in Extended Data Table 3.
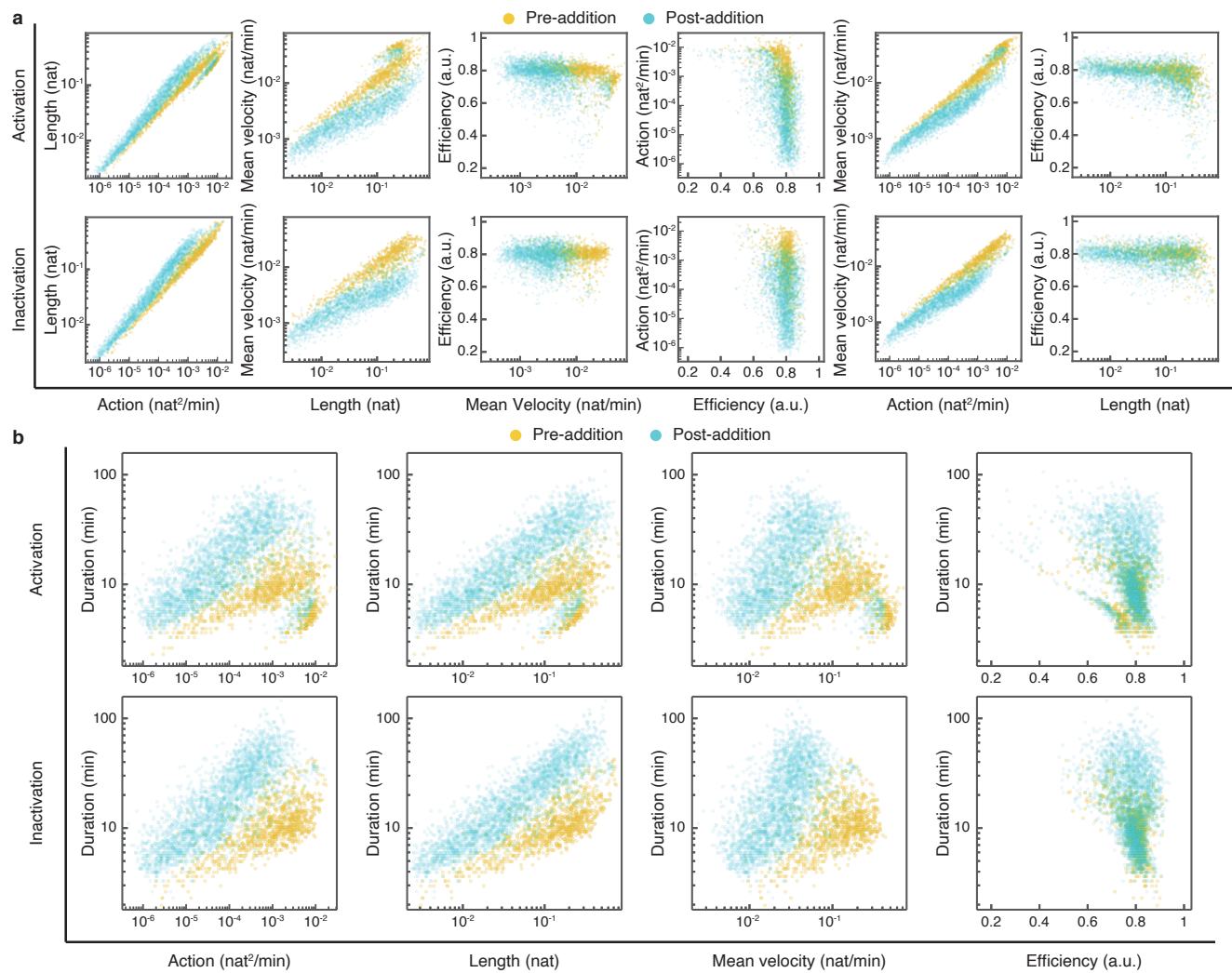
Extended Data Figure 4: The correlation between two information-geometric quantities before and after the Raf inhibitor addition. **a** The scatter plots of the action $\mathcal{C}$, the length $\mathcal{L}$, the mean velocity $\mathcal{V}$, the efficiency η before (pre-addition) and after (post-addition) the Raf inhibitor addition. **b** The scatter plots of the duration $t_1 - t_0$ versus the action $\mathcal{C}$, the length $\mathcal{L}$, the mean velocity $\mathcal{V}$, the efficiency η before (pre-addition) and after (post-addition) the Raf inhibitor addition. The Pearson correlation coefficients and results of statistical tests are listed in Extended Data Table 4.

Extended Data Table 1: The sample size used in the analysis of each experiment. We listed the sample size for the experiments under the conditions of different cell densities and the experiments of the periods before and after the Raf inhibitor addition.

Condition	Number of cells	Number of activation	Number of inactivation
Low density (L)	31	507	513
Medium density (M)	306	3,130	3,131
High density (H)	755	4,425	4,029
Before the Raf inhibitor addition (Pre)	209	1,085	978
After the Raf inhibitor addition (Post)	209	2,716	2,628

Extended Data Table 2: The statistics for the experiment at each cell density (related to Fig. 3 and Extended Data Fig. 1). **a** The mean values (Mean) and variances (Variance) of the action $\mathcal{C}$, the length $\mathcal{L}$, the mean velocity $\mathcal{V}$, the efficiency η, and the duration $t_1 - t_0$ in the activation and inactivation processes at the low (L), medium (M) and high (H) cell densities. **b** The mean values (Mean) and variances (Variance) of ds^2/dt^2, $d/dt(ds^2/dt^2)$, and $\left|d/dt(ds^2/dt^2)\right|$ in the activation and inactivation processes at the low (L), medium (M) and high (H) cell densities. **c** The p-values comparing between two cases. We used Brunner-Munzel (BM) method and the Kolmogorov–Smirnov (KS) method. We compare two cell densities and two processes, where 'vs' denotes the comparison of two cases, and L, M and H denotes the low, medium and high cell densities. The p-values below 0.001 represent as < 0.001.

a

		$\mathcal{C}$		$\mathcal{L}$		$\mathcal{V}$		η		$t_1 - t_0$	
		Activation	Inactivation	Activation	Inactivation	Activation	Inactivation	Activation	Inactivation	Activation	Inactivation
Mean	L	0.00580	0.00339	0.201	0.192	0.0319	0.0221	0.751	0.760	7.17	8.58
	M	0.0105	0.00642	0.243	0.236	0.0453	0.0313	0.740	0.770	6.30	8.03
	H	0.0156	0.00828	0.327	0.344	0.0493	0.0272	0.690	0.714	7.93	12.6
Variance	L	0.0000957	0.0000159	0.0219	0.0216	0.000847	0.0000848	0.00808	0.00694	17.1	26.2
	M	0.000224	0.000116	0.0320	0.0328	0.00152	0.000598	0.00869	0.00662	14.0	28.2
	H	0.000364	0.0000572	0.0431	0.0461	0.00145	0.000158	0.0129	0.0109	16.8	33.3

b

		$\frac{ds^2}{dt^2}$		$\frac{d}{dt}\frac{ds^2}{dt^2}$		$\left|\frac{d}{dt}\frac{ds^2}{dt^2}\right|$	
		Activation	Inactivation	Activation	Inactivation	Activation	Inactivation
Mean	L	0.00162	0.000789	-0.000409	-0.00000359	0.00161	0.000671
	M	0.00332	0.00160	-0.000791	0.0000228	0.00356	0.00136
	H	0.00394	0.00132	-0.000480	-0.00000405	0.00375	0.000807
Variance	L	0.0000300	0.00000155	0.0000492	0.00000146	0.0000467	0.00000101
	M	0.0000852	0.0000263	0.000139	0.0000356	0.000127	0.0000337
	H	0.0000965	0.00000464	0.000109	0.00000293	0.0000952	0.00000228

c

		Activation			Inactivation			Activation vs Inactivation		
		L vs M	L vs H	M vs H	L vs M	L vs H	M vs H	L	M	H
$\mathcal{C}$	BM	< 0.001	< 0.001	< 0.001	< 0.001	< 0.001	< 0.001	< 0.001	< 0.001	< 0.001
	KS	< 0.001	< 0.001	< 0.001	< 0.001	< 0.001	< 0.001	< 0.001	< 0.001	< 0.001
$\mathcal{L}$	BM	< 0.001	< 0.001	< 0.001	< 0.001	< 0.001	< 0.001	0.261	0.0877	0.00455
	KS	< 0.001	< 0.001	< 0.001	< 0.001	< 0.001	< 0.001	0.253	0.0120	0.00134
$\mathcal{V}$	BM	< 0.001	< 0.001	< 0.001	< 0.001	< 0.001	< 0.001	< 0.001	< 0.001	< 0.001
	KS	< 0.001	< 0.001	< 0.001	< 0.001	< 0.001	< 0.001	< 0.001	< 0.001	< 0.001
η	BM	0.0573	< 0.001	< 0.001	0.0463	< 0.001	< 0.001	0.356	< 0.001	< 0.001
	KS	0.0573	< 0.001	< 0.001	0.0178	< 0.001	< 0.001	0.356	< 0.001	< 0.001
$t_1 - t_0$	BM	< 0.001	< 0.001	< 0.001	0.00480	< 0.001	< 0.001	< 0.001	< 0.001	< 0.001
	KS	< 0.001	< 0.001	< 0.001	0.00480	< 0.001	< 0.001	0.00480	< 0.001	< 0.001
$\frac{ds^2}{dt^2}$	KS	< 0.001	< 0.001	< 0.001	< 0.001	< 0.001	< 0.001	< 0.001	< 0.001	< 0.001
$\frac{d}{dt}\frac{ds^2}{dt^2}$	KS	< 0.001	< 0.001	< 0.001	< 0.001	< 0.001	< 0.001	< 0.001	< 0.001	< 0.001
$\left|\frac{d}{dt}\frac{ds^2}{dt^2}\right|$	KS	< 0.001	< 0.001	< 0.001	< 0.001	< 0.001	< 0.001	< 0.001	< 0.001	< 0.001

Extended Data Table 3: The statistics for the experiment of the Raf inhibitor addition (related to Fig. 3 and Extended Data Fig. 1). **a** The mean values (Mean) and variances (Variance) of the action $\mathcal{C}$, the length $\mathcal{L}$, the mean velocity $\mathcal{V}$, the efficiency η, and the duration $t_1 - t_0$ in the activation and inactivation processes before (Pre) and after (Post) the Raf inhibitor addition. **b** The mean values (Mean) and variances (Variance) of ds^2/dt^2, $d/dt(ds^2/dt^2)$, and $\left|d/dt(ds^2/dt^2)\right|$ in the activation and inactivation processes before (Pre) and after (Post) the Raf inhibitor addition. **c** The p-values comparing between two cases, before (Pre) and after (Post) the Raf inhibitor addition. We used Brunner-Munzel (BM) method and the Kolmogorov–Smirnov (KS) method. We calculated the p-values for the action $\mathcal{C}$, the length $\mathcal{L}$, the mean velocity $\mathcal{V}$, the efficiency η, the duration $t_1 - t_0$, ds^2/dt^2, $d/dt(ds^2/dt^2)$, and $\left|d/dt(ds^2/dt^2)\right|$. The p-values below 0.001 represent as < 0.001.

a

		$\mathcal{C}$		$\mathcal{L}$		$\mathcal{V}$		η		$t_1 - t_0$	
		Activation	Inactivation	Activation	Inactivation	Activation	Inactivation	Activation	Inactivation	Activation	Inactivation
Mean	Pre	0.00279	0.00207	0.159	0.169	0.0181	0.0138	0.775	0.792	9.42	11.5
	Post	0.000713	0.000345	0.0954	0.0882	0.00494	0.00311	0.756	0.781	20.1	22.7
Variance	Pre	0.0000131	0.00000656	0.0147	0.0185	0.000204	0.0000696	0.00394	0.00298	23.6	39.0
	Post	0.00000269	0.000000872	0.0129	0.0119	0.0000505	0.0000064	0.00861	0.00439	229	320

b

		$\frac{ds^2}{dt^2}$		$\frac{d}{dt}\frac{ds^2}{dt^2}$		$\left|\frac{d}{dt}\frac{ds^2}{dt^2}\right|$	
		Activation	Inactivation	Activation	Inactivation	Activation	Inactivation
Mean	Pre	0.000593	0.000362	-0.000143	-3.88×10^{-8}	0.000269	0.000131
	Post	0.0000710	0.0000303	-0.0000174	-2.50×10^{-9}	0.0000257	0.00000640
Variances	Pre	0.00000166	0.000000300	0.000000321	4.59×10^{-8}	0.000000269	2.88×10^{-8}
	post	0.000000133	1.06×10^{-8}	2.37×10^{-8}	4.86×10^{-10}	2.34×10^{-8}	4.45×10^{-10}

c

		Activation	Inactivation
		Pre vs Post	Pre vs Post
$\mathcal{C}$	BM	< 0.001	< 0.001
	KS	< 0.001	< 0.001
$\mathcal{L}$	BM	< 0.001	< 0.001
	KS	< 0.001	< 0.001
$\mathcal{V}$	BM	< 0.001	< 0.001
	KS	< 0.001	< 0.001
η	BM	< 0.001	< 0.001
	KS	< 0.001	< 0.001
$t_1 - t_0$	BM	< 0.001	< 0.001
	KS	< 0.001	< 0.001
$\frac{ds^2}{dt^2}$	KS	< 0.001	< 0.001
$\frac{d}{dt}\frac{ds^2}{dt^2}$	KS	< 0.001	< 0.001
$\left|\frac{d}{dt}\frac{ds^2}{dt^2}\right|$	KS	< 0.001	< 0.001

Extended Data Table 4: The Pearson correlation coefficients and the p-values (related to Extended Data Figs. 2, 4). **a** The Pearson correlation coefficients for the logarithm of information-geometric quantities, the action $\mathcal{C}$, the length $\mathcal{L}$, the mean velocity $\mathcal{V}$, the logarithm of the duration $t_1 - t_0$ and the efficiency η in the activation and inactivation processes at the low (L), medium (M) and high (H) cell densities. **b** The Pearson correlation coefficients for the logarithm of information-geometric quantities, the action $\mathcal{C}$, the length $\mathcal{L}$, the mean velocity $\mathcal{V}$, the logarithm of the duration $t_1 - t_0$ and the efficiency η before (Pre) and after (Post) the Raf inhibitor addition. **c** The p-values of no correlation test based on the Pearson correlation coefficients for the conditions, i.e., the low (L), medium (M) and high (H) cell densities, and before (Pre) and after (Post) the Raf inhibitor addition. We calculated the p-values for the logarithm of information-geometric quantities, the action $\mathcal{C}$, the length $\mathcal{L}$, the mean velocity $\mathcal{V}$, the logarithm of the duration $t_1 - t_0$ and the efficiency η. The p-values below 0.001 represent as < 0.001.

a

		$\ln\mathcal{C}$ vs $\ln\mathcal{L}$	$\ln\mathcal{L}$ vs $\ln\mathcal{V}$	$\ln\mathcal{V}$ vs η	$\ln(t_1-t_0)$ vs $\ln\mathcal{C}$	$\ln\mathcal{C}$ vs $\ln\mathcal{V}$	$\ln\mathcal{L}$ vs η	$\ln\mathcal{V}$ vs $\ln(t_1-t_0)$	η vs $\ln\mathcal{C}$	$\ln\mathcal{L}$ vs $\ln(t_1-t_0)$	$\ln\mathcal{C}$ vs $\ln(t_1-t_0)$
L	Activation	0.925	0.612	-0.0618	0.286	0.857	-0.280	-0.240	-0.297	0.621	0.286
	Inactivation	0.951	0.561	0.156	0.637	0.776	-0.132	0.0196	-0.141	0.838	0.637
M	Activation	0.934	0.679	-0.154	0.195	0.889	-0.403	-0.269	-0.395	0.525	0.195
	Inactivation	0.944	0.616	0.0310	0.508	0.833	-0.237	-0.0474	-0.230	0.758	0.508
H	Activation	0.921	0.622	-0.0758	0.109	0.865	-0.441	-0.395	-0.407	0.474	0.109
	Inactivation	0.962	0.684	-0.0802	0.594	0.841	-0.456	0.0772	-0.445	0.780	0.594

b

		$\ln\mathcal{C}$ vs $\ln\mathcal{L}$	$\ln\mathcal{L}$ vs $\ln\mathcal{V}$	$\ln\mathcal{V}$ vs η	$\ln(t_1-t_0)$ vs $\ln\mathcal{C}$	$\ln\mathcal{C}$ vs $\ln\mathcal{V}$	$\ln\mathcal{L}$ vs η	$\ln\mathcal{V}$ vs $\ln(t_1-t_0)$	η vs $\ln\mathcal{C}$	$\ln\mathcal{L}$ vs $\ln(t_1-t_0)$	$\ln\mathcal{C}$ vs $\ln(t_1-t_0)$
Pre	Activation	0.978	0.894	-0.334	0.315	0.966	-0.402	0.0642	-0.422	0.504	0.315
	Inactivation	0.987	0.907	-0.0813	0.68	0.961	-0.282	0.454	-0.245	0.787	0.680
Post	Activation	0.973	0.851	-0.441	0.570	0.945	-0.455	0.277	-0.516	0.740	0.570
	Inactivation	0.986	0.888	-0.158	0.818	0.949	-0.223	0.600	-0.247	0.901	0.818

c

		$\ln\mathcal{C}$ vs $\ln\mathcal{L}$	$\ln\mathcal{L}$ vs $\ln\mathcal{V}$	$\ln\mathcal{V}$ vs η	$\ln(t_1-t_0)$ vs $\ln\mathcal{C}$	$\ln\mathcal{C}$ vs $\ln\mathcal{V}$	$\ln\mathcal{L}$ vs η	$\ln\mathcal{V}$ vs $\ln(t_1-t_0)$	η vs $\ln\mathcal{C}$	$\ln\mathcal{L}$ vs $\ln(t_1-t_0)$	$\ln\mathcal{C}$ vs $\ln(t_1-t_0)$
L	Activation	< 0.001	< 0.001	0.165	< 0.001	< 0.001	< 0.001	< 0.001	< 0.001	< 0.001	< 0.001
	Inactivation	< 0.001	< 0.001	0.00155	< 0.001	< 0.001	0.00558	0.658	0.00420	< 0.001	< 0.001
M	Activation	< 0.001	< 0.001	< 0.001	< 0.001	< 0.001	< 0.001	< 0.001	< 0.001	< 0.001	< 0.001
	Inactivation	< 0.001	< 0.001	0.0831	< 0.001	< 0.001	< 0.001	0.0160	< 0.001	< 0.001	< 0.001
H	Activation	< 0.001	< 0.001	< 0.001	< 0.001	< 0.001	< 0.001	< 0.001	< 0.001	< 0.001	< 0.001
	Inactivation	< 0.001	< 0.001	< 0.001	< 0.001	< 0.001	< 0.001	< 0.001	< 0.001	< 0.001	< 0.001
Pre	Activation	< 0.001	< 0.001	< 0.001	< 0.001	< 0.001	< 0.001	0.0346	< 0.001	< 0.001	< 0.001
	Inactivation	< 0.001	< 0.001	0.0110	< 0.001	< 0.001	< 0.001	< 0.001	< 0.001	< 0.001	< 0.001
Post	Activation	< 0.001	< 0.001	< 0.001	< 0.001	< 0.001	< 0.001	< 0.001	< 0.001	< 0.001	< 0.001
	Inactivation	< 0.001	< 0.001	< 0.001	< 0.001	< 0.001	< 0.001	< 0.001	< 0.001	< 0.001	< 0.001

Supplementary Video 1: The fluorescence imaging of the phosphorylated ERK in NRK-52E cells at different cell densities. The movies of the low (left), medium (middle), and high (right) densities are arranged in order from the left. The pseudo-color indicates the FRET/CFP ratio, where the green (red) color indicates that the FRET/CFP ratio is 1.0 (2.0) (see also Fig. 2**c**). The timestamps indicate the time from imaging initiation in minutes.

Supplementary Video 2: The fluorescence imaging of the phosphorylated ERK in NRK-52E cells with the Raf inhibitor addition. The Raf inhibitor was added at time 120 min. The pseudo-color indicates the FRET/CFP ratio, where the green (red) color indicates that the FRET/CFP ratio is 1.0 (2.0) (see also Fig. 2**c**). The timestamp indicates the time from imaging initiation in minutes.